COO-2107-11

Contract E(11-1)-2107

CORRELATION OF SUBSTRUCTURE WITH MECHANICAL PROPERTIES OF PLASTICALLY DEFORMED REACTOR STRUCTURAL MATERIALS

F A T I G U E

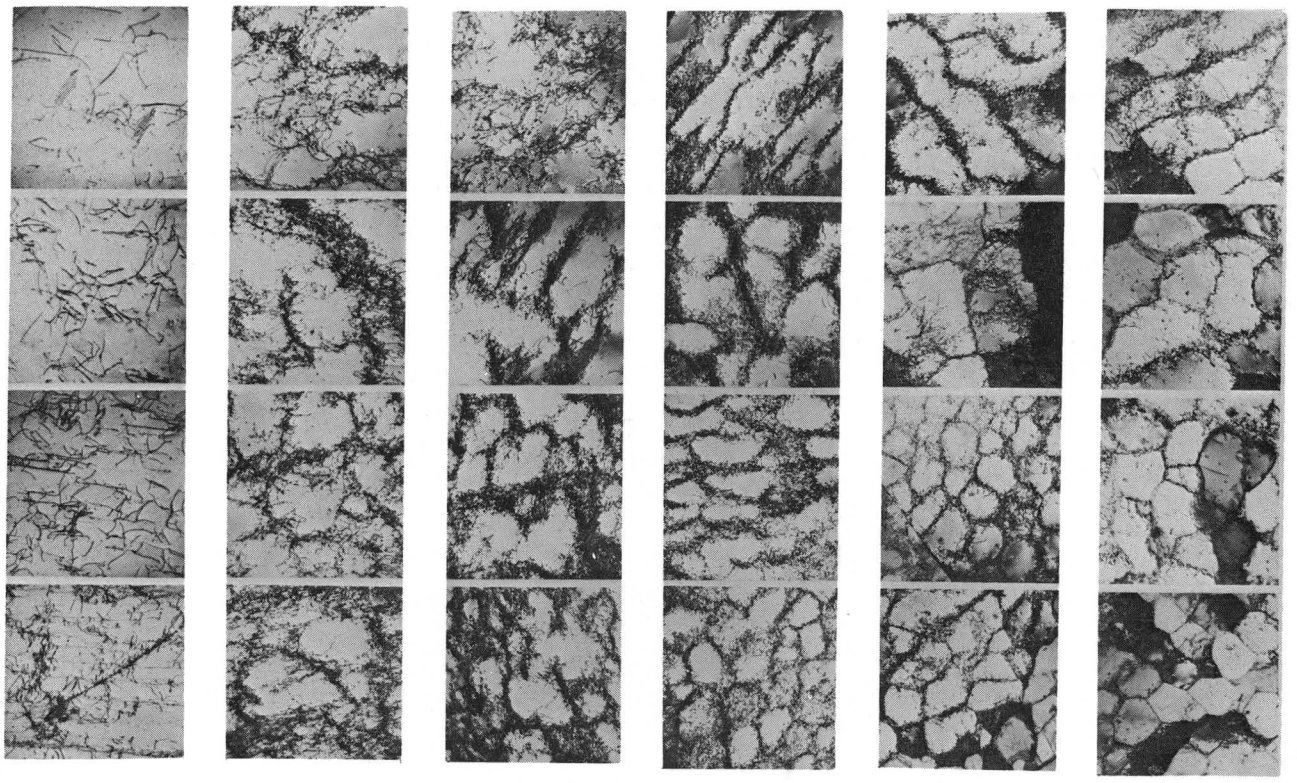

3/4 Cycles 2 3/4 Cycles 6 3/4 Cycles 80 Cycles 361 Cycles N_f=722 Cycles

PROGRESS REPORT

Period January 1, 1974 to December 31, 1975

J. Moteff, Principal Investigator
Department of Materials Science and Metallurgical Engineering

March 15, 1976

University of Cincinnati
Cincinnati, Ohio 45221

DISCLAIMER

TABLE OF CONTENTS

		Page
	LIST OF FIGURES	v
	SUMMARY	viii
I	OBJECTIVE	1
II	INTRODUCTION	1
III	EXPERIMENTAL PROGRAM	2
	A. Monotonic Deformation Mode (Tensile, Creep)	2
	1. Some Aspects of Dislocation Mechanisms During Creep of AISI 316 and 304 Stainless Steel	2
	2. Characterization of the Creep and Tensile Substructure of 304 Stainless Steel, Reference Heat 9T2796	5
	3. Analysis of Relationships of Deformation Rate, Stress and Temperature for 304 Stainless Steel	7
	4. Estimation of Activation Energy for Creep from Hot Hardness Measurements of 304 Stainless Steel	9
	5. Characterization of the Substructure During Early Stages of Creep of 304 Stainless Steel.	11
	6. The Role of Twin Boundary - Grain Boundary Intersections on Microcracking Behavior of AISI 304 Stainless Steel Deformed in Slow Tension and Creep at 650°C, Reference Heat 9T2796	13
	7. Intragranular Deformation Behavior of AISI 304 Stainless Steel at Elevated Temperature, Reference Heat 9T2796	16
	8. Substructure Strengthening of Room Temperature Mechanical Properties in Incoloy 800 and AISI 304 Stainless Steel	21

Page

B. Cyclic Deformation Mode 22

1. Substructure Development During Low Cycle Fatigue of AISI 304 Stainless Steel at 649°C, Reference Heat 9T2796 22

2. Comparison of the Fatigue Properties in Incoloy 800 When Tested in the Bend and Push-Pull Modes 26

3. The Effect of Creep - Fatigue Interaction on the Substructure and Fracture Characteristics in 304 Stainless Steel 29

IV PLANS FOR FUTURE WORK 31

V REFERENCES 32

VI DISTRIBUTION LIST 36

APPENDIX I . . . . . I-A

COVER PAGE PHOTOGRAPH

The series of transmission electron micrographs on the cover of this report shows the substructural development of AISI 304 stainless steel. Hour glass specimens were fatigued to different fractions of fatigue life at 649°C under a total strain range of 2%. Each column of micrographs shows the variation in substructure that can occur within a given specimen after the indicated number of cycles. It is apparent that the cell intercept size decreases until the saturation state is reached and that the misorientation angle between adjacent cells and the volume fraction occupied by cells increase throughout the fatigue life. The saturation state was reached at about thirty cycles. The magnification of this cover picture is $\sim$ 7,000 X. Further details are described in section B.1. of this report.

LIST OF FIGURES

Figure

1 The Ratio ρ_{sb}/ρ_m in Steady-State and Tertiary State Creep Plotted Against τ/Gb for 316 Stainless Steel.

2(a) Density of Dislocations Bound in Sub-Boundaries, ρ_{sb}, as a Function of Creep Strain for 316 Stainless Steel.

2(b) The Ratio ρ_{sb}/ρ_m in Steady-State and Tertiary State as a Function of Creep Strain for 316 Stainless Steel.

3 Mobile Dislocation Density Versus Creep Strain for 304 Stainless Steel Tested at 593°C and at an Applied Stress of 30 ksi.

4 Typical Substructure Developed in Creep Tested AISI 304 Stainless Steel (Heat 9T2796) at (a) 816°C, 52 MPa; (b) 760°C, 69 MPa; (c) 704°C, 103 MPa; and 760°C, 138 MPa.

5 Typical Substructure Developed in AISI 304 Stainless Steel (Heat 9T2796) (a) 649°C, 172 MPa, creep; (b) 704°C, $\dot{\varepsilon} = 8.3 \times 10^{-5}$ sec^{-1}, tensile; (c) 538°C, 276 MPa, creep; and (d) 649°C, $\dot{\varepsilon} = 8.3 \times 10^{-5}$ sec^{-1}, tensile.

6 Typical Substructure Developed in AISI 304 Stainless Steel (Heat 9T2796) Tested in Tension at (a) and (b) 538°C, $\dot{\varepsilon} = 8.3 \times 10^{-5}$ sec^{-1}, (c) 593°C, $\dot{\varepsilon} = 8.3 \times 10^{-5}$ sec^{-1}; and (d) 649°C, $\dot{\varepsilon} = 8.3 \times 10^{-4}$ sec^{-1}.

7 Typical Substructure Developed in AISI 304 Stainless Steel (Heat 9T2796) Tested in Tension at a Strain Rate $\dot{\varepsilon} = 8.3 \times 10^{-2}$ sec^{-1} at (a) 538°C; (b) 593°C; (c) 649°C; and (d) 704°C.

8 Plot of the Cell of Subgrain Intercept Size, λ, vs. the Modulus Compensated True Stress, σ_T/G on a log-log Scale (AISI 304 Stainless Steel).

9 Plot of the Modulus Compensated True Stress, σ_T/G, vs. the Square Root of the Dislocation Density, $\rho^{1/2}$, AISI 304 SS, (Reference Heat 9T2796).

10 Plot of the Misorientation Angle, θ, vs. the Subgrain Intercept Size, λ (AISI 304 SS).

Figure

11-A Plot of the Natural Log of the Deformation Rate, $\dot{\varepsilon}$, vs. the Natural Log of the Modulus Compensated Stress, σ_T/E. (AISI 304 Stainless Steel, Reference Heat 9T2796).

11-B Plot of the Temperature Compensated Deformation Rate, Z, vs. the Modulus Compensated Stress, σ_T/E, on a ℓn-ℓn Scale. (AISI 304 Stainless Steel, Reference Heat 9T2796).

12 Plot of Hardness/Young's Modulus Ratio as a Function of Reciprocal Temperature for 304 Stainless Steel, Heat Number 9T2796.

13 Strain Behavior in 304 SS as a Function of Time During Creep at 704°C with Corresponding Dislocation Substructures. (Stress 17.58 $kg \cdot mm^{-2}$).

14 Plot of the Misorientation Angle, θ, vs. the Strain, ε, of AISI 304 SS (Heat G8607) Creep Tested at 704°C.

15 Plot of the Cell or Subgrain Intercept Size, λ, vs. the Modulus Compensated True Stress, σ_T/G (AISI 304 SS, Heat G8607).

16 Schematics Showing Various Types of Cracks.

17 Distribution of Intergranular Cracks Associated with Twin Boundary - Grain Boundary Intersection (TGI) as a Function of Deformation Rate.

18 Angular Percentage Distribution of Different Types of Intergranular Cracks: (a) Type c and e; (b) Type i, j and k; (c) Type g to k in Reference to Fig. 16.

19 Distribution of Grain Intercepts in the Undeformed Region of a Tensile Tested Specimen ($\dot{\varepsilon}_t = 8.33 \times 10^{-4}$ sec^{-1}) of AISI 304 Stainless Steel (9T2796).

20 Intragranular Elongation as a Function of Grain Intercept for the Family of Tensile (a) and Creep (b) Tested Specimens of AISI 304 (9T2796) at 650°C.

21 Room Temperature Hardness as a Function of Reciprocal of Cell or Subgrain Intercepts.

22 Plot of the Total Stress Range, $\Delta\sigma$, Versus the Number of Cycles, N, for AISI 304 Stainless Steel at 649°C.

Figure

23 Low Cycle Fatigue Substructure Development in AISI 304 Stainless Steel at 649°C.

24 Plot of the Subboundary Intercept Size, λ, Versus the Fraction of Fatigue Life, N/N_f for AISI 304 Stainless Steel at 649°C.

25 The Shear Modulus Compensated Cyclic Stress Amplitude, σ/G, as a Function of the Corrected Reciprocal of the Subboundary Intercept Size, b/λ, for AISI 304 Stainless Steel at 649°C.

26 Plot of the Misorientation Angles Between Adjacent Cells, θ, Against the Fraction of Fatigue Life, N/N_f, for AISI 304 Stainless Steel at 649°C.

27 Transverse Hardness Distribution in Incoloy 800 of Bend Fatigue Specimen on Plane Parallel to Fracture Surface with Corresponding Substructure.

28 Diametrical Hardness Distribution in Incoloy 800 of Push-Pull Fatigue Specimen on Plane Parallel to Fracture Surface with Corresponding Substructure.

29 Influence of Maximum Cyclic Tensile Stress on the Subboundary Intercept Size for 304 Stainless Steel Tested at 650°C in the Fatigue Mode with Various Tensile Hold Times.

30 Diagram-Plot of Characteristic Subgrain Diameters Associated with Various Tensile Hold Periods for 0.5% and 2.0% Total Strain Ranges.

31 Diagram-Plot of Cycles to Failure Versus Various Tensile Hold Periods for 0.5% and 2.0% Total Strain Ranges, Showing the Saturation in Cycles to Failure and the Transgranular to Intergranular Propagation with Increasing Tensile Hold Period.

SUMMARY

The interactions between the dislocations which form the subgrain boundaries and those which are sufficiently mobile to contribute to creep deformation are evaluated. The ratio of the dislocations in the sub-boundaries, ρ_{SB}, to those dislocations, ρ_m, within the subgrains is found to be independent of the applied stress and the creep strain once the steady-state creep stage has been reached.

Characterization of creep and tensile substructure of type 304 stainless steel (Reference Heat 9T2796) specimens shows a strong correlation of the observed cell or subgrain sizes with the flow stress of the alloy. At modulus compensated stress levels below $\sim 2 \times 10^{-3}$, the substructure takes the form of well defined subgrains with the size, λ, in microns, varying as

$$\lambda = 6.6b(\sigma_T/E)^{-1}$$

where σ_T is the effective true stress, E is Young's Modulus and b the Burgers vector. For stresses above this critical value, cells are formed the size-stress relationship being given by

$$\lambda = 1.4 \times 10^{-2} b(\sigma_T/E)^{-2}.$$

The deformation rate-stress relation for the 304 stainless steel is shown to follow a power law of the form

$$\dot{\varepsilon} = B \lambda^3 (\sigma_T/E)^n \exp(-Q_c/RT)$$

where λ is the subgrain or cell intercept size, Q_c an activation energy with a value of $\sim$ 85 kcal/mole, B is a constant. It is found that n takes the value of 7 at σ_T/E lower than $\sim 2 \times 10^{-3}$ and of 10.5 for σ_T/E higher than $\sim 2 \times 10^{-3}$.

Evaluation of activation energy for creep from hot hardness measurements shows a value of 87 kcal/mole, which is in reasonable agreement with the value of 85 kcal/mole obtained from tensile and creep data.

TEM evaluations of the substructure were performed on a set of specimens of 304 stainless steel tested in creep at 704°C to study the development of the substructure as a function of creep strain. Well developed subgrains were observed for specimens tested till rupture and the subgrain size-stress relationship determined for the reference heat adequately describes the results from this heat.

The role of twin boundary-grain boundary intersections (TGI) on microcracking behavior of type 304 stainless steel deformed in slow tension and creep at 650°C has been investigated. The number of cracks associated with TGI are shown to increase with decreasing strain rate. It is concluded that TGI may behave in a similar manner to grain boundary triple junctions in the cracking process in the sense that TGI provide the barrier to crack propagation as well as the convenient crack nucleation sites.

Grain shape analysis was employed to study how the individual grains behave and contribute to tensile and creep strain of 304

stainless steel at 650°C. Preliminary results indicate that the intragranular deformation becomes more predominant in the grains with the larger intercept distances. It is also shown that the grain boundary sliding becomes important as the strain rate decreases, consistent with the previous study on micro-cracking process in this alloy.

The room temperature mechanical properties of austenitic stainless steels were found to be enhanced by the introduction of cells or subgrains formed during high temperature deformation with a following relationship:

$$H = H_o + k \lambda^{-1}$$

where H is the room temperature microhardness, H_o is the frictional hardness, λ is the subboundary intercept distance and k is a constant.

The substructural development during high temperature low cycle fatigue of type 304 stainless steel has been investigated by transmission electron microscopy. Hour glass type specimens have been tested to different fractions of fatigue life under a total strain range of 2% with a cyclic strain rate of 4×10^{-3} sec^{-1} at 649°C. Cells were observed to form within 0.4% of the fatigue life well before the onset of the saturation state which was reached after $\sim$ 4% of the fatigue life. It was also found that the cell intercept size decreases until the saturation state is reached and that the misorientation angle between adjacent

cells and the volume fraction occupied by cells increase throughout the fatigue life. The observations are discussed in terms of the recent theoretical predictions and it is suggested that the subboundary movement might account for the cyclic strain.

A study on the comparison of the fatigue properties and substructure when tested in the bend and push-pull mode of Incoloy 800 is nearing completion. A concept based on crack nucleation and growth is used to explain the differences in fatigue lives when comparisons are made between the bend and push-pull fatigue tests at low strain ranges. Significant substructural variation is found to exist in accordance with the stress or strain distribution in the bend fatigue specimen. Consequently, it is suggested that special care should be exercised in evaluating the fatigue substructure of bend fatigue specimens.

A study to investigate the effect of hold time on the fatigue substructure and fracture characteristics in 304 stainless steel is nearing completion. Preliminary results show that quantifiable interrelations might exist between the fatigue properties, substructural observations and failure behavior.

I. OBJECTIVE

The objective of this program is to (a) evaluate the time, temperature and stress-dependent mechanical properties of reactor structural materials, (b) determine the relationship of these properties to the microstructure, (c) show the contribution of the microstructure to the internal stress fields and the subsequent influence on microcracking and the grain boundary sliding behavior during the normal plastic deformation at elevated temperatures and (d) demonstrate the relationship of the hot micro-hardness properties with the hot-tensile properties of a class of commercial and advanced alloys presently under investigation at other laboratories. Special consideration is being given to operating conditions typical of nuclear reactor applications, including the knowledge that radiation environment can influence the substructure of these metals, a circumstance which can lead to significant changes in the conventional mechanical property behavior.

II. INTRODUCTION

Transmission electron microscopy has been used as the primary tool to study the deformation substructure of reactor structural materials resulting from creep, fatigue and tensile testing at elevated temperatures. Complementary work using optical microscopy, scanning electron microscopy and hot-hardness testing has been performed to characterize the deformation and failure behavior.

New work being initiated will also include similar studies on the Commercial, the Developmental and the Fundamental alloys being evaluated in the National Alloy Developmental Program with particular attention on the application of hot-hardness measurement as a strength microprobe.

III. EXPERIMENTAL PROGRAM

Since the work at the University of Cincinnati has been contributed to "Mechanical Properties Test Data for Structural Materials Quarterly Progress Reports" of Oak Ridge National Laboratory[1-9], a condensed description of research activities over the two year period from January 1, 1974 to December 31, 1975 is presented here in this biannual report.

The experimental program is divided into parts using A) monotonic deformation mode and B) cyclic deformation mode categories. Each part is subdivided into various mini-research programs for convenience.

A. Monotonic Deformation Mode (Tensile, Creep)

A.1. Some Aspects of Dislocation Mechanisms During Creep of AISI 316 and 304 Stainless Steel (H. Nahm and V. K. Sikka*)

It is well known that some metals and alloys exhibit subgrain formation during creep process. However, the interaction between those dislocations going into the subgrain boundary and those presently in the subgrain boundary is not well known because of

*Now with the Metals and Ceramics Division of Oak Ridge National Laboratory.

its complexity.

As a start, the creep rate can be presented by:

$$\dot{\varepsilon} = \alpha\rho b\bar{v} \qquad [1]$$

where α is a geometrical factor, ρ the mobile dislocation density, b the Burgers vector, and $\bar{v}$ is the average dislocation velocity. The total dislocation density can be written as:

$$\rho_t = \rho_{sb} + \rho_m \qquad [2]$$

where ρ_t is the total dislocation density, ρ_{sb} is the dislocation density forming the subgrain boundary and ρ_m is the dislocation in the subgrain. The average dislocation velocity, as well as, the dislocation density tends to change during deformation, especially in the transient stage of deformation. At this time, the internal stress increases due to the formation of subgrains, increase in the number of forest dislocations, etc.

In order to develop a better understanding of the dislocation interactions during creep, a preliminary analysis based on the theoretical approach taken by Orlova and Cadek[10] was made. This study deals with the dislocations which form the subgrain boundaries in AISI 316 stainless steel[11] and also compares with other parameters, including the dislocation substructure of AISI 304 stainless steel as a function of creep strain.

The dislocation density forming the subgrain boundary, ρ_{sb}, is assumed to be following the relationship:

$$\rho_{sb} = \frac{3\theta}{b\lambda'} \qquad [3]$$

where θ is the misorientation angle between the subgrains, b is the Burger's vector and λ' is the mean subgrain diameter.

It was found that the dislocation density within the subgrain, ρ_m, and that in the boundaries, ρ_{sb} can be expressed as a power function of the parameter consisting of the true shear stress, divided by the Burger's vector, τ/Gb with an exponent value of 2.

The dislcoation density ratio ρ_{sb}/ρ_m for steady-state creep of 316 stainless steel has been observed to be independent of both the parameter τ/Gb and the creep strain. This tendency is shown in Figure 1 and 2. The dislocation density ratio ρ_{sb}/ρ_m has a value of 4.2 for stainless steel, similar to that observed for pure metals[12]. Based on the present analysis, the recovery in steady-state for 316 stainless steel is suggested to take place by mutual annihilation of free dislocations and not by entry of these dislocations into sub-boundaries.

Figure 3 shows the relationship between the mobile dislocation density and creep strain for AISI 304 stainless steel at 593°C with an applied stress of 30 ksi. A factor of 10^3 decrease in the creep strain rate (i.e. the product of the mobile dislocation density and the dislocation velocity) observed for the case of 304

stainless steel during the period of time immediately following the application of the load to the onset of steady-state is accounted for by a factor of $\sim$ 5 due to a decrease in the dislocation density needed to form the subboundaries and a factor of $\sim$ 200 due to the decrease in the average dislocation velocity caused by the increase in the internal stress as a result of the presence of the sub-boundaries and forest dislocations.

Details of this work are available[13] elsewhere and work is still progressing in this area.

A.2. Characterization of the Creep and Tensile Substructure of 304 Stainless Steel, Reference Heat 9T2796 (R. K. Bhargava)

The dislocation substructure of the tensile and creep tested specimens of AISI 304 stainless steel (Reference Heat 9T2796) was evaluated by transmission electron microscopy. The test conditions of these specimens involved a temperature range of 538°C to 816°C and the strain rates varied from 9.7×10^{-9} sec^{-1} to 8.3×10^{-2} sec^{-1}. The stress levels of these specimens varied from 34.5 MPa (5,000 psi) to 385 MPa (55,800 psi).

The detailed descriptions of TEM dislocation substructure and its quantitative data have been reported in the ORNL Quarterly Progress Reports[3,4,6,7]. Therefore only a brief summary is presented in this report.

Typical substructures developed in tensile and creep mode at elevated temperatures are shown in Figures 4 thru 7. Figure 4

shows that well defined subgrains are developed in specimens tested at low stresses and relatively high temperatures in the creep mode. The substructure that is developed in creep at higher stresses and low temperatures and in slow tension at relatively higher temperatures consists of elongated subgrains and elongated cells respectively (Figure 5). The substructure consisted of irregular patches of cell walls and cells were observed to form in the tensile specimens tested at high strain rates as shown in Figures 6 and 7.

Figure 8 shows a plot of the cell or subgrain intercept size, λ, versus the modulus compensated true stress, σ_T/G on a log-log scale. For comparison with the present results, the data obtained by Cuddy[14] for creep substructure in a type 304 stainless steel have also been plotted in the same figure. The cell or subgrain size - stress relationships determined for the reference heat 9T2796 seem to provide a very good fit to Cuddy's data. In Figure 9 the modulus compensated true stress, σ_T/G is plotted versus the square root of the dislocation density, $\rho^{0.5}$, on a linear scale. The data can be represented by a straight line confirming the various work hardening theories. The stress - dislocation density relation is given by

$$\sigma_T/G = - 6.67 \times 10^{-4} + 1.97\ b\ \rho^{0.5} \qquad [4]$$

The constant and the slope were determined by a least square analysis of the data. The misorientation angle across the subgrain

boundaries, θ, is plotted versus the cell or subgrain intercept size, λ, in Figure 10. The misorientation angle seems to be independent of the subgrain size.

A.3. Analysis of Relationships of Deformation Rate, Stress and Temperature for 304 Stainless Steel (R. K. Bhargava)

In order to understand the deformation behavior of 304 stainless steel at elevated temperatures in the light of the substructure the tensile and creep test data (ORNL data as reported by R. W. Swindeman, ORNL Metals and Ceramics Division) have been analyzed. The dislocation substructure that is developed in the tensile and creep tested specimens has been evaluated by TEM and the results have been presented in the preceding section, A.2.

In Figure 11-A the deformation rate, $\dot{\varepsilon}$ (minimum creep rate for creep tests and the nominal strain rates in the tensile tests), at various temperatures has been plotted versus the modulus compensated true stress parameter, σ_T/E on a ℓn-ℓn scale. Figure 11-B shows a plot of the temperature compensated deformation rate, Z and the modulus compensated true stress parameter, σ_T/E on a ℓn-ℓn scale. The power law

$$\dot{\varepsilon} = A(\sigma_T/E)^n \exp(-Q_c/RT) \qquad [5]$$

with $n = 7$ and $Q_c = 85{,}000$ cals/mole describes the rate-stress relationship at lower stress values for all temperatures. The

value of n starts to increase from 7 at σ_T/E values in the range of 1.5×10^{-3} to 2.0×10^{-3} for different temperatures. The behavior at very high strain rates and lower temperatures has been discussed before[5,15] in the light of the dislocation substructure. For most of the data, if the power law is assumed to be followed at higher stresses ($\sigma_T/E > 1.9 \times 10^{-3}$), the value of $\underline{n}$ lies between 10 and 11 (Figure 11-B).

Cuddy[14] and Yu[16] have reported that for type 304 stainless steel the value of the stress exponent, $\underline{n}$, ranges between 5 and 13. For pure metals and solid solution alloys where subgrains form during creep, the value of $\underline{n}$ usually lies between 4 and 5. Higher values of $\underline{n}$ have also been observed for tungsten[17] and aluminum[18,19]. Sherby and co-workers[17,19] have suggested an explanation for the high value of $\underline{n}$ by explicitly incorporating the influence of subgrains in the creep deformation equations. A similar approach is utilized in the following explanation of the results of the present study.

Creep rate at a constant temperature is given by

$$\dot{\varepsilon}_s = \text{Constant } \lambda^p \sigma^N \qquad [6]$$

where λ is the subgrain size, N is the stress exponent determined from differential tests where λ and T are kept constant and p is usually 2 or 3. According to a model of subgrain creep wherein pile ups of dislocations were considered to interact with subgrain boundaries, Weertman[20] arrived at the equation

$$\dot{\varepsilon}_s = \text{Constant} \cdot \lambda^3 \cdot (\sigma/G)^6 \qquad [7]$$

where G is the shear modulus.

In the light of the substructure that is developed, the deformation rate - stress relationship for the present result is adequately described by

$$\dot{\varepsilon}_s = \text{Constant}\ \lambda^3 \cdot (\sigma_T/E)^n \exp \frac{85,000}{RT} \qquad [8]$$

where $n = 7$ at σ_T/E values lower than about 1.9×10^{-3} and $n = 10.5$ for $\sigma_T/E > 1.9 \times 10^{-3}$. At lower stress levels where the subgrain size, λ, is given by

$$\lambda = 6.6b\ (\sigma_T/E)^{-1} \qquad [9]$$

the value of $\underline{n}$ becomes 4 and at higher stress levels where the λ - σ_T/E relation is given by

$$\lambda = 1.4 \times 10^{-2}\ b\ (\sigma_T/E)^{-2} \qquad [10]$$

$\underline{n}$ in Eq. [8] reduces to 4.5.

The value of $\underline{n}$ after considering the influence of subgrain or cells reduces from 7 or 11 to 4 or 4.5 and agrees very well with the usually observed values for the stress exponent during power law creep[21].

A.4. Estimation of Activation Energy for Creep from Hot Hardness Measurements of 304 Stainless Steel (R. K. Bhargava)

The room temperature and elevated temperature mechanical

properties of AISI 304 stainless steel are being studied very extensively, especially on the reference heat 9T2796.

A small sample of this reference heat was given an anneal at 1093°C for one-half hour and then electropolished in preparation for the measurement of hot hardness. The hardness in terms of DPH units were measured from RT to 1300°C. The details of the hot hardness apparatus are given elsewhere[22]. The specimen was held at the test temperature for 15 minutes before the indents were made.

The temperature variation of hardness may be given by a relation of the type:

$$H = A \exp(Q'/T) \qquad [11]$$

In order to obtain Q', the apparent activation energy in units of calories per mole, Larsen-Badse[23] used the equivalent relationship:

$$H = A \exp(2Q'/RT) \qquad [12]$$

where R is the gas constant. The apparent activation energy Q' has been correlated to the activation energy for creep or self diffusion.

Sherby and Armstrong[24] suggested the relation:

$$H/E = B \exp(Q_L/nRT) \qquad [13]$$

where Q_L is lattice self diffusion activation energy, E is the Young's modulus, n is the stress exponent for creep (usually n = 5) and B is a material constant. H in Eq. [13] is the hot hardness above 0.75 T_m.

The H/E values are plotted versus $10^3/T$ in Figure 12. As can be seen clearly, the data below and above $\sim$ 0.75 T_m can be fit by two straight lines. The break in the curve around 0.75 T_m signifies a change in mechanism of deformation and is probably associated with the power law breakdown as suggested by Sherby and Armstrong.

The activation energy, Q, is calculated utilizing Eq. [13] and n = 5. The value of Q = 87 kcals/mole is in reasonable agreement with the 84 kcal/mole used in the creep analysis. This value of Q is in reasonable agreement with the published values in the literature. Garofalo et. al.[25] determined an activation energy for creep and reported 75 kcals/mole whereas Cuddy[14] reported a value of 91±9 kcals/mole for the creep activation energy. Work is continuing in the correlation of hot hardness data with macroscopic mechanical properties at elevated temperatures.

A.5. Characterization of the Substructure During Early Stages of Creep of 304 Stainless Steel (R. K. Bhargava)

To characterize the substructural development during creep, 304 stainless steel specimens were terminated at different creep strains under identical test conditions and subsequently, the

developed substructure was examined by transmission electron microscopy. Details of this study are available elsewhere[5,6], therefore, some of the results will be presented here.

Figure 13 shows the typical micrographs of the substructure developed during the various stages of creep deformation. Also included is the substructure before testing for comparison. The dislocation density before testing was estimated at $(7.4 \pm 0.4) \times 10^8$ cm^{-2}. On loading, the dislocation density increases to a value of $(7.14 \pm 0.84) \times 10^9$ cm^{-2}. The photo micrograph (RUC-6) shows some loops, stacking faults and some tangled and free dislocations. In the early primary stage (RUC-3), the dislocation density increases to $(9.94 \pm 0.86) \times 10^9$ cm^{-2}. The typical substructure consists of more tangles with some localized tendency to form cells. In the late primary stage (RUC-4), the tendency to form cells became more prevalent. The total dislocation density remained more or less the same. During steady state creep (RUC-5), the substructure started to take on the shape of subgrains with definite subgrain boundaries. Again the dislocation density remained the same. Finally at rupture (RUC-10) a well developed subgrain substructure was formed. There was some variation in the subgrain size, the size being smaller near grain boundaries.

The misorientation between the adjacent subgrains or cells was also measured and are presented in Figure 14. This shows a plot of the average misorientation versus the total strain. This value of strain is determined from the section used for the TEM

study. The data from this study indicates an increase in the misorientation as the strain increases. After the secondary stage has developed, the increase in misorientation angle is less apparent and it tends to reach a saturation value. The average subgrain intercept, λ, is plotted versus the modulus compensated true stress, σ_T/G in Figure 15. For comparison the relationship determined for the reference heat 9T2796 is also shown. Work is continuing in this area for the other alloy systems.

A.6. The Role of Twin Boundary - Grain Boundary Intersections on Microcracking Behavior of AISI 304 Stainless Steel Deformed in Slow Tension and Creep at 650°C, Reference Heat 9T2796 (H. Nahm)

Studies of intergranular crack formation in metals at elevated temperatures have shown that triple points may provide both preferential sites for the nucleation of cracks and barriers to their propagation[26-30]. Although it has been shown that the growth of cracks originating at grain boundary triple junctions may be arrested or interrupted at twin boundary - grain boundary intersections[31,32], relatively little is known concerning the influence of these intersections on the crack propagation process in austenitic stainless steel.

Recent work has shown evidence for the formation of cracks and cavities along twin boundaries in 304 stainless steel[33]. These results suggest that the twin boundaries may behave in a

manner similar to grain boundaries under the proper conditions.

The purpose of this study is to report quantitative observations concerning the influence of twin boundary - grain boundary intersections (hereafter referred to as TGI) on the intergranular cracking behavior in AISI 304 stainless steel deformed in the slow tension and creep rupture modes at 650°C. Figure 16 describes the crack morphology that will be used in this analysis.

The distribution of cracks terminated at TGI's and secondary cracks associated with TGI's are plotted in Figure 17 as a function of deformation rate. It is apparent that both the intergranular cracks related to TGI's and the secondary cracks increase with decreasing deformation rate (i.e. decreasing stress levels). This is consistent with the overall intergranular crack results for these specimens where triple junctions are involved[30].

There is a strong indication that the propagation of triple point cracks may be interrupted at TGI's. This is mainly based on the observation that there are non-negligible number of triple point cracks which occupy sites between triple points and TGI (as shown in Figure 16-c, e, and Figure 17). Although it is difficult to visualize the actual cracking process, it can be safely assumed that the intergranular cracks have a greater tendency to nucleate at or near the triple point and then proceed toward the TGI and the next triple point. This circumstance may be explained from the fact that the surface energy[34], and stress concentration

due to the applied stress at triple junctions are higher than those at TGI's. The majority of cracks observed are triple point cracks which again supports this idea. Figure 18-A shows the angular incidence with respect to the applied stress of triple point cracks which are filled between the triple junction and TGI (Figure 16-c). Cracks with a length of less than one boundary facet are plotted in this Figure. The angular orientation of these cracks is consistent with those triple point cracks which are not associated with TGI[30].

There is a further experimental result indicating that the secondary cracks appear, at times, to originate from TGI. Approximately 1 - 3 percent of the total population of cracks observed in each specimen are found to be secondary cracks which occupy sites between TGI. And the 1 - 4 percent are found to be those lying between TGI and boundaries not associated with TGI (Figure 16-i, k). From the above observations, it is concluded that the role of the TGI appears to be similar to that of the triple joint junction in the normal cracking process.

In one study of secondary cracks which were formed in copper, Gittins and Williams[35] suggested that the secondary cracking may be affected by the triple point cracking because of the plastic strain field ahead of the triple point cracks. However, in this study of 304 stainless steel, careful examination shows that there is a predominance of secondary cracks formed along the boundary facet where no triple point cracks were observed to occur. Further-

more, as shown in Figure 18-b and c, the angular orientation of secondary cracks shows the same behavior as that of triple point cracks[30]. From the preceding observations together with the result that the considerable number of secondary cracks are related to TGI, it appears that the secondary cracking mode is essentially the same as the triple point cracking mode. It is a reasonable conclusion since the role of TGI is quite similar to that of triple junction in the cracking behavior. It would be especially true in the case of coarse grain size materials such as the 210 μm size employed in this study. This cracking behavior could be different in fine grain size materials because there are more triple points available sites for cracking.

Details of the present study were provided previously[3] and a further study of this area is underway with particular attention to the fracture mechanisms at elevated temperatures.

A.7. Intragranular Deformation Behavior of AISI 304 Stainless Steel At Elevated Temperature, Reference Heat 9T2796 (H. Nahm)

The effect of grain size on creep properties of metals and alloys has been studied by many investigators. Theoretical and empirical relationships have been proposed to attempt to explain the role of grain size on the complex high temperature deformation process. For example, based on the concept of different mobile dislocation densities which may be present in the various grains of different sizes, Garofalo[36] proposed the equation:

$$\dot{\varepsilon}_s = \frac{A_1}{d} + A_2 d^2 \qquad [14]$$

where $\dot{\varepsilon}_s$ is the secondary creep rate, d is the grain size and A_1 and A_2 are constants. Barrett, Lytton and Sherby[37] suggested an equation of the type:

$$\dot{\varepsilon}_s = k(\lambda/d)\ \dot{\varepsilon}_{gb} + [1-k(\lambda/d)]\ \dot{\varepsilon}_i \qquad [15]$$

where $\dot{\varepsilon}_s$ is the secondary creep rate, k is a constant, λ is the subgrain size, d is the grain size, $\dot{\varepsilon}_{gb}$ is the grain boundary sliding rate and $\dot{\varepsilon}_i$ is the intragranular deformation rate. Eq. [15] was obtained from the considerations that the deformation is more significant near the grain boundary than inside the grain, and the total grain boundary area per unit volume of the specimen becomes larger as the grain size becomes smaller.

Recently Gifkins[38] developed a theoretical expression for the creep rate, $\dot{\varepsilon}_s$, given as follows:

$$\dot{\varepsilon}_s = \dot{\varepsilon}_i + \dot{\varepsilon}_i\ (2Kw\ \lambda/d^2) \qquad [16]$$

where $\dot{\varepsilon}_i$ is the intragranular deformation rate, K and w are the stress concentration factor and the width of the fold at the triple point respectively, λ is the subgrain size and d is the grain size. This was derived by considering the climb - controlled accommodation of grain boundary sliding due to the triple point fold formation, together with the climb-controlled intragranular deformation.

Most studies on the effect of grain size, including the preceding three equations, are based on the assumption that the metals or alloys considered have a uniform distribution of the grains with a constant given diameter. It should be realized, however, that there will be a distribution in grain sizes and one usually reports only the average size of the grains.

It is, therefore, quite informative to find how the individual grains behave and contribute to the overall deformation at elevated temperature. The purpose of this section is to report the preliminary results from the study on the deformation behavior of the individual grains by grain shape analysis. The details of this study were described previously[4].

The modified grain shape analysis by Hensler and Gifkins[40] was used on the six specimens of 304 stainless steel (9T2796) which were tested in tension and creep-rupture modes at 650°C. The deformation rates covered were between 8.33×10^{-4} sec^{-1} and 4.16×10^{-8} sec^{-1}, which correspond the stress range from 42 ksi to 15 ksi. The chemistry and the testing results are available elsewhere[30]. The grain intercept of six specimens was 180 ± 5μm. This was obtained from the measurement of more than 500 intercepts of the shoulder portion of each specimen.

Intragranular elongation, $\dot{\varepsilon}_i$, was obtained from the equation:

$$\dot{\varepsilon}_i = (L/\bar{W})^{2/3} - 1 \qquad [17]$$

where L is the average length of the grain and $\bar{W}$ is the average width of the grain, with respect to the stress axis. More than 800 grains were measured individually in terms of the length (L) and the width ($\bar{W}$) for each specimen. The grain intercept was determined from

$$d = \frac{L + \bar{W}}{2} \qquad [18]$$

and the intragranular elongation was calculated for the grains with 50μm intervals such as d is from 0∿50μm, 50∿100μm, 100μm ∿ 150μm, etc.

The distribution of grain intercepts with intervals of 50μm as a function of relative frequencies measured is given in Figure 19. This was obtained from the underformed section (button-head) of a tensile specimen ($\dot{\varepsilon} = 8.33 \times 10^{-4}$ sec^{-1}) with more than 1300 grains measured. As can be shown in Figure 19, even in the same specimen with the average grain intercept dimension of ∿ 180μm, there is a wide range of distribution of different grain sizes. The distribution shows the positive skewness, i.e. there are more small grains than large grains.

Figure 20 shows the intragranular elongations as a function of grain intercept intervals of 50μm from the deformed regions of the respective specimens. Several important observations can be noted. The intragranular deformation is a strong function of the grain size and it becomes more significant as the strain rate increases. In other words, the influence of grain size diminishes

as the deformation rate decreases. For example, no appreciable change in the intragranular deformation can be noted for the case where the grain intercept, d, is larger than 100μm at the 4.16×10^{-8} sec^{-1} deformation rate, while at the 8.33×10^{-4} sec^{-1} the intragranular deformation increases as the grain size increases to values up to more than 400μm. One more result can be drawn from the data presented in this figure and that is that grain boundary sliding becomes important as the deformation rate decreases as noted by comparing the total elongation and the intragranular elongation. This observation is consistent in the studies of McLean, Garofalo, etc., and with the previous results on microcracking behavior on these identical specimens[30] in the sense that microcracking increases as the deformation rates is decreased.

The present result as shown in Figure 20 is undoubtedly complex and not easily explained. However, it appears that the different deformation mechanisms might be operative in this wide range of strain rates, considering the previous microcracking behavior on these specimens[30,33,39]. At higher strain rates the grain size strengthening appears to be important, similar to the case of the grain size effect on the room temperature property. As the strain rate decreases, the grain boundary sliding becomes more important and the reasonings contained in Eqs. [15] and [16] or the interpretation by Matlock and Nix[41] could be applied. This phenomenon becomes even more important in the evaluation of the embrittlement observed in irradiated stainless steels, a case where

the matrix of the grain is hardened and grain boundary sliding is significantly reduced. Detailed analysis comprising the subgrain dimension on these observations is still underway at this laboratory.

A.8. Substructure Strengthening of Room Temperature Mechanical Properties in Incoloy 800 and AISI 304 Stainless Steel

(H. Nahm and R. K. Bhargava)

In a recent study[42], the ambient temperature mechanical properties have been shown to be enhanced via high temperature substructure strengthening. To further study this behavior, room temperature hardness measurements were made on the specimens having different cell or subgrain sizes developed from the previous high temperature deformation. The hardness variation is shown in Figure 21. From this figure, it is clearly shown that the relationship holds as

$$H = H_o + k \lambda^{-1} \qquad [19]$$

where H_o corresponds to the frictional hardness parameter. This is quite consistent with the relationship

$$\sigma = \sigma_o + k \lambda^{-1} \qquad [20]$$

where σ_o is the frictional stress. One point to note here is that the hardness appears to deviate from its linearity approaching a saturation when the λ^{-1} parameter increases as shown in Figure 21.

This trend, with decreasing cell size, will be confirmed in future studies.

B. Cyclic Deformation Mode

B.1. Substructure Development During Low Cycle Fatigue of AISI 304 Stainless Steel at 649°C, Reference Heat 9T2796 (H. Nahm)

In an effort to understand the basic principles underlying fatigue, substructure development during fatigue has been investigated by many researchers. However, most investigations have been concerned with fatigue in single crystals at ambient temperatures. It appears that no study is available in the literature on the substructural changes at different stages of fatigue life at elevated temperature where recovery becomes increasingly important. The purpose of the present study is, therefore, to examine the dislocation substructure development in low cycle fatigued AISI type 304 stainless steel at 649°C by transmission electron microscopy. Details of this study were reported before[7].

A special set of LCF tests were performed at Argonne National Laboratory, Materials Science Division, High Temperature LCF Laboratory under the provisions of a "Thesis Parts Program". The tested specimens of AISI 304 stainless steel (9T2796) were solution treated at 1092°C for half an hour and aged for 1,000 hours at 593°C.

The hour glass type specimens have been tested to different

fractions of the fatigue life under the identical testing conditions of temperature (649°C), total strain range (2%) and cyclic strain rate (4×10^{-3} sec^{-1}).

A plot of stress range, $\Delta\sigma$, versus the number of cycles, N, for AISI 304 stainless steel is presented in Figure 22. Several remarks can be made from this figure. Excellent reproducibility of hardening behavior, under identical experimental conditions, is obtained especially at the saturation stage. The difference at the initial stages of hardening is believed to be due to the difference in the initial microstructures that results from the ageing treatment. But the difference decreases as cycling continues so the saturation stresses for each specimen are almost identical. The rapid hardening stage is finished in around 30 cycles followed by the saturation state where the flow stress remains constant until fatigue failure sets in.

The characteristics of the fatigue substructure development are summarized with a series of micrographs as shown in Figure 23. Each column of micrographs show the variation in substructure that can occur within a given specimen after the indicated number of cycles. It is apparent that the cell intercept size, λ, decreases until the saturation state is reached and the misorientation angle, θ, between adjacent cells and the volume fraction occupied by cells increase throughout the fatigue life.

Cell intercept size, λ, as a function of fatigue life, N/N_f is plotted in Figure 24. The shear modulus compensated cyclic

stress amplitude, σ/G, is plotted in Figure 25 as a function of the corrected reciprocal of cell intercept size, b/λ, where b is the Burgers vector taken to be 2.54×10^{-8} cm. An equation of the type

$$\sigma/G = A\,(b/\lambda)^{n} \qquad [21]$$

is obtained, which indicates that the cell size decreases with increasing stress.

A plot of average misorientation angles between adjacent cells, θ, against fractions of fatigue life, N/N_f, is provided in Figure 26 showing that the present result of the misorientation increases throughout fatigue life.

As shown in Figure 23 the early hardening stage is attained through the continuous accumulation of dislocations in the form of dipoles, multipoles, and loops that form uncondensed cell walls. The decrease in cell size until the saturation state is another way of dislocation storage contributing to the hardening. During the saturation state, most of the flow stress is gained from either the stress for dislocations to move through the long range stress field set up by subboundaries or the stress needed to bow out dislocations between the dislocation network of sub-boundary. It is evident that recovery is occurring during the entire fatigue process. This is manifested by the observation that the misorientation angles increase and the uncondensed thick cell walls continuously refine themselves throughout the

entire fatigue life.

It is in order at this point to discuss what mechanisms account for the cyclic strain in fatigue, especially in saturation state. If we assume that "cell shuttling" model[43-45] is operating, a relationship

$$\gamma = \rho b \lambda' \qquad [22]$$

should be true, where γ is the shear strain range, b is the Burgers vector, and λ' is the subgrain diameter. Substitution of the present results for AISI 304 stainless steel into Eq. [22] indicates that around 50 shuttling dislocations per cell are needed to accomodate the strain range for each cycle during saturation stage. This is contradictory to the observation that the region inside the subgrain is almost free from dislocations. Therefore, the cell shuttling model does not appear to adequately explain the straining during saturation stage of fatigue. Feltner[46] proposes a similar model in which the "flip-flop" motion of dislocation loops yield the same result as in the case of the cell shuttling model.

Therefore, the preceeding discussions lead to another mechanism-movement of subboundary walls during deformation. Cell walls can bulge out under complex cooperative stress system as suggested by Li[47]. Or cell walls can annihilate each other and/or glide under the proper conditions as proposed by Ashby, et. al.[48].

It is also possible that the annihilation of dislocations by

recovery near or in the subboundary walls may be partly responsible for the cyclic strain, especially in the early hardening stage. The observed transition for cell walls from the thick, uncondensed to condensed, sharp and narrow walls along with the continuous increase in the misorientation angles supports this data.

B.2. Comparison of the Fatigue Properties in Incoloy 800 When Tested in the Bend and Push-Pull Modes (H. Nahm and A. Ermi)

In order to better interpret and to apply the results of experimental data of elevated temperature mechanical properties, it is important to understand the testing technique and the specimen geometry employed in the various types of deformation modes. It is also very important to know which microstructural changes will affect the mechanical properties.

With the above objectives in mind, fatigue properties and their correlation with dislocation structures in Incoloy 800 have been studied on the specimens tested in push-pull and in bend fatigue modes at elevated temperatures. Experimental details and fatigue properties such as strain ranges and cycles to failure have been reported before[49]. Fatigue lives from bend fatigue were found to compare very well with those from push-pull fatigue, especially at large strain ranges. It was also shown that bend-fatigue test specimens with small strain ranges yield longer fatigue life than the push-pull fatigue specimens. The bend-fatigue test

is different from the push-pull in the sense that the former is cantiliver-loaded. Thus, the bend-fatigue specimens have maximum strain or stress at the specimen surface which decreases toward the center and becomes zero at the neutral axis.

Room temperature microhardness was measured on the polished and etched surface cut parallel to the fracture surface. Figures 27 and 28 illustrate the hardness distribution and corresponding dislocation substructure, from just below the fracture and along the diameter from the center for the push-pull fatigue specimen, respectively. As expected the hardness reveals the characteristics of each testing condition. Bend fatigue specimens reveal the minimum hardness along the neutral axis and the maximum on both surfaces. In contrast to bend fatigue, no change in hardness can be observed in these specimens tested in the push-pull mode (Figure 28).

Transmission electron microscopy revealed substructural characteristics that are consistent with the hardness distribution. Figure 27 illustrates the structural variation as a function of the position on a plane parallel to the neutral axis. Dislocation density increases as one moves from the neutral axis (essentially zero strain region) to the specimen surface where the maximum strain exists ($\Delta\varepsilon_t \simeq 2\%$). A modulated dislocation substructure consisting of cells is formed near the surface. The dislocation density obtained from the unstressed shoulder portion is around 5.5×10^8 cm^{-2}. In principle, the dislocation density in the neutral axis should

be the same as that of the unstressed portion, but the observed difference is apparently due to the fact that neutral axis continuously shifts during cyclic reverse bending, thereby inducing a small amount of residual stress in the form of dislocation. It is also interesting to note that the existence of a critical dislocation density for cell formation can be seen from Figure 27.

Compared to the case of bend fatigue, there is little change in deformation substructure across the guage section diameter of the hour-glass push-pull fatigue specimen shown in Figure 28. Stress and strain distribution on the minimum cross section seem to have uniform value during the push-pull fatigue testing.

The fact that bend fatigue test invariably yields a longer fatigue life than does push-pull fatigue in the small range could be explained from the differences in crack growth rate and in time spent for crack nucleation and growth[50]. For the case of the large strain range test, most of the fatigue life is spent for crack propagation, i.e., time for crack nucleation is short and once nucleated, the crack will propagate rapidly, giving a good correlation between bend and push-pull fatigue. But for the case of bend fatigue tests with small strain ranges, most of the fatigue life is spent in crack nucleation. Because of the stress gradient along the specimen, the crack growth rate becomes lower toward the neutral axis of the bend fatigue specimen,

resulting in a longer fatigue life.

As demonstrated in Figures 27 and 28, there is a significant difference in hardness distribution and dislocation substructure in bend fatigue specimen. Thus, extreme care should be exercised when the fatigue substructure is evaluated in the specimens tested in bend-fatigue mode.

A new work has been also initiated to study the crack initiation/propagation in Incoloy 800 at elevated temperature via scanning electron microscopy on the same specimens discussed here and the results will be given in the future reports.

B.3. The Effect of Creep - Fatigue Interaction on the Substructure and Fracture Characteristics in 304 Stainless Steel (T. Kenfield*)

A study was initiated to characterize the effect of hold time on LCF behavior in 304 stainless steel. Specifically, the substructure was investigated using transmission electron microscopy to obtain the correlation of mechanical properties with the sub-grain intercept size. In addition to this substructure analysis, fractography was performed using scanning electron microscopy and replica microscopy to study the mode of cracking. Specimens were tested at 649°C at two different strain ranges (0.5%, 2%) with various tension hold times ranging from one minute up to ten hours. Details of this study are available elsewhere[51].

Figure 29 shows the relationship between the subboundary

*Now with General Electric Company, Sunnyvale, California.

intercept size, λ, and the maximum cyclic tension stress, $\sigma_{t,max}$, the slope of the plot being -2 which gives a dependency of

$$\lambda \propto \sigma_{t,max}^{-2} \qquad [23]$$

This correlation is in general agreement with that found for cell formation in tensile[15,52] as well as, the fatigue data for 316 stainless steel[53]. It is also shown that smaller subgrains are formed in specimens tested at lower strain ranges at the same stress levels, shifting the data to the left. This is consistent with the previous results[53].

Figure 30 shows the substructural characteristics for the specimens with various tensile hold times. It is apparent that the subboundary intercept size increases with longer hold periods, reflecting the stress relaxation phenomena in the specimens. It can be also noted that the nature of the subboundary changes from cells to subgrains as the hold period is increased. This indicates that the creep type damage becomes predominant, as evidenced by the fact that cells are often observed in tensile tested specimens while subgrain structures are found in creep tested specimens. Carbide formation also appears to become important in specimens with a very long hold period as shown in this figure.

In order to get an insight into the possible correlation between the substructure and the failure mechansims, fracture surface was studied by scanning electron microscope. The number

of cycles to failure, N_f, is plotted in Figure 31 against the hold times with the corresponding fractographs. This shows the transition from transgranular to intergranular failure mode with the increasing tensile hold time. This is consistent with the substructural observation shown in Figure 30. It is also worth noting that the tendency for intergranular fracture is enhanced with the lowering strain ranges. Further study is underway to clarify the deformation and failure mechanism in the area of creep-fatigue interaction.

IV. PLANS FOR FUTURE WORK

A new program has been initiated on the Commercial, the Developmental and the Fundamental Alloys being evaluated in the National Alloy Development Program. Particular attention will be given to the application of hot-hardness measurement as a strength microprobe, in addition to the studies by combinations of transmission and scanning electron microscopy and experiments in which tensile and creep tests are performed.

The scope of the work will include the following areas:

1. Creep-microstructure evaluation of two (AISI 330, A286) of the candidate advanced commercial alloys from Activity B of the National Alloy Development Program (NADP).
2. Hot-hardness measurements on the eight alloys presently being evaluated in Activity B (Commercial Alloys) of the NADP.

3. Hot-hardness measurements on the eight alloys presently being evaluated in Activity C (Developmental Alloys) of the NADP.
4. Hot-hardness measurements of a family of alloys to be identified from Activity D (Fundamental Studies) of the NADP.

Work will continue on the characterization of the substructure formed during the strain-controlled push-pull fatigue test of Incoloy 800. Further analyses and discussions of the substructure data for Incoloy 800 will be performed. Special attention will be given on the effect of strain range on the subgrain dimension and the dislocation density.

A new study on difference in fatigue-cracking (initiation/propagation) in Incoloy 800 when tested in bend and push-pull modes is underway by scanning electron microscopy.

V. REFERENCES

1. ORNL-4948, "Mechanical Properties Test Data for Structural Materials", Quarterly Progress Report for Period Ending January 31, 1974.
2. ORNL-4963, "Mechanical Properties Test Data for Structural Materials", Quarterly Progress Report for Period Ending April 30, 1974.
3. ORNL-4998, "Mechanical Properties Test Data for Structural Materials", Quarterly Progress Report for Period Ending July 31, 1974.
4. ORNL-5103, "Mechanical Properties Test Data for Structural Materials", Quarterly Progress Report for Period Ending October 31, 1974.

5. ORNL-5104, "Mechanical Properties Test Data for Structural Materials", Quarterly Progress Report for Period Ending January 31, 1975.

6. ORNL-5105, "Mechanical Properties Test Data for Structural Materials", Quarterly Progress Report for Period Ending April 30, 1975.

7. ORNL-5106, "Mechanical Properties Test Data for Structural Materials", Quarterly Progress Report for Period Ending July 31, 1975.

8. ORNL-5107, "Mechanical Properties Test Data for Structural Materials", Quarterly Progress Report for Period Ending October 31, 1975.

9. ORNL-5112, "Mechanical Properties Test Data for Structural Materials", Quarterly Progress Report for Period Ending January 31, 1976.

10. A. Orlova and J. Cadek, Phil. Mag. 28, 891 (1973).

11. K. D. Challenger and J. Moteff, Met. Trans. 4, 749 (1973).

12. J. E. Bailey and P. B. Hirsch, Phil. Mag. 5, 485 (1960).

13. V. K. Sikka, H. Nahm and J. Moteff, Mat. Sci. Eng. 20, 55 (1975).

14. L. J. Cuddy, Met. Trans. 1, 395 (1970).

15. R. K. Bhargava, R. W. Swindeman and J. Moteff, "Correlation of the Microstructures with the Creep and Tensile Properties of AISI 304 Stainless Steel", Proceedings of a Symposium on "Structural Materials for Service at Elevated Temperatures in Nuclear Power Generations", edited by A. O. Schaefer, Published by ASME, December 1975, pp. 31-54.

16. C. C. Yu, M. S. Thesis, 1973, University of Cincinnati.

17. S. L. Robinson and O. D. Sherby, Acta Met., 17, 109 (1969).

18. S. K. Mitra and D. McLean, Met. Sci. J., 1, 192, (1967).

19. S. L. Robinson, C. M. Young and O. D. Sherby, J. Mat. Sci., 9, 341 (1974).

20. J. Weertman, "High Temperature Creep Produced by Dislocation Motion", presented at John Dorn Memorial Symposium, Cleveland,

Ohio, October 1972.

21. O. D. Sherby and P. M. Burke, Progress in Mat. Sci., 13, 235 (1968).

22. J. L. Kamphouse, J. C. Blake and J. Moteff, Rev. Sci. Instr. 40, 321 (1969).

23. Jorgen Larson-Badge, Trans. Japan Inst. Metals 9, 312 (1968).

24. O. D. Sherby and P. E. Armstrong, Met. Trans. 2, 3479 (1971).

25. F. Garofalo, O. Richmond, W. F. Domis and F. von Gemminger, Jt. Inter. Conf. on Creep, 1, 31 (1963).

26. U. Lindborg, Acta Met. 17, 157 (1969).

27. U. Lindborg and B. O. Gustafsson, Fracture 1969 (ed. P.L. Pratt), Chapman and Hall, London, p. 457 (1969).

28. R. Soderberg, Fracture 1969 (ed. P. L. Pratt), Chapman and Hall, London, p. 450 (1969).

29. J. S. Waddington and K. Lofthouse, J. Nucl. Mat. 22, 205 (1967).

30. H. Nahm, D. J. Michel and J. Moteff, J. Mat. Sci. 8, 104 (1973).

31. D. McLean, J. Inst. of Metals 85, 468 (1957).

32. C. W. Weaver, J. Inst. of Metals, 87, 126 (1959).

33. D. J. Michel, H. Nahm and J. Moteff, Mat. Sci. Eng. 11, 97 (1973).

34. L. E. Murr, G. I. Wong and R. J. Horylev, Acta Met. 21, 595 (1973).

35. A. Gittins and J. A. Williams, Scripta Met., 3, 209 (1969).

36. F. Garofalo, et. al., Trans. AIME, 230, 1460 (1964).

37. C. R. Barrett, J. L. Lytton and O. D. Sherby, Trans. AIME, 239, 170 (1967).

38. Gifkins, J. Aust. Inst. Met., 18, 137 (1973).

39. H. Nahm and J. Moteff, J. Mat. Sci., 10, 1084 (1975).

40. J. H. Hensler and R. C. Gifkins, J. Inst. Met., 92, 340 (1963-64).

41. D. K. Matlock and W. D. Nix, Met. Trans., 5, 961 (1974).

42. C. M. Young and O. D. Sherby, JISI, 211, 640 (1973).

43. D. F. Watt and R. K. Ham, Nature (London) 211, 734 (1966).

44. S. J. Basinski, Z. S. Basinski and A. Howie, Phil. Mag., 19, 899 (1969).

45. J. R. Hancock and J. C. Grosskreutz, Acta. Met., 17, 77 (1969).

46. C. E. Feltner, Phil. Mag., 12 1229 (1965).

47. J. C. M. Li, "Electron Microscopy and Strength of Crystals", Edited by G. Thomas, et. al., Interscience, New York, p. 713 (1963).

48. M. F. Ashby and R. A. Verrall, Acta Met., 21 149 (1973).

49. Progress Report, April thru December, 1973, COO-2107-10, March 15, 1974, University of Cincinnati, Cincinnati, Ohio.

50. S. S. Manson, Exper. Mechs., July, 193 (1964).

51. T. A. Kenfield, M. S. Thesis, 1974, University of Cincinnati.

52. D. J. Michel, J. Moteff and A. J. Lovell, Acta Met., 21, 1269 (1973).

53. K. D. Challenger and J. Moteff, Met. Trans., 3, 1675 (1972).

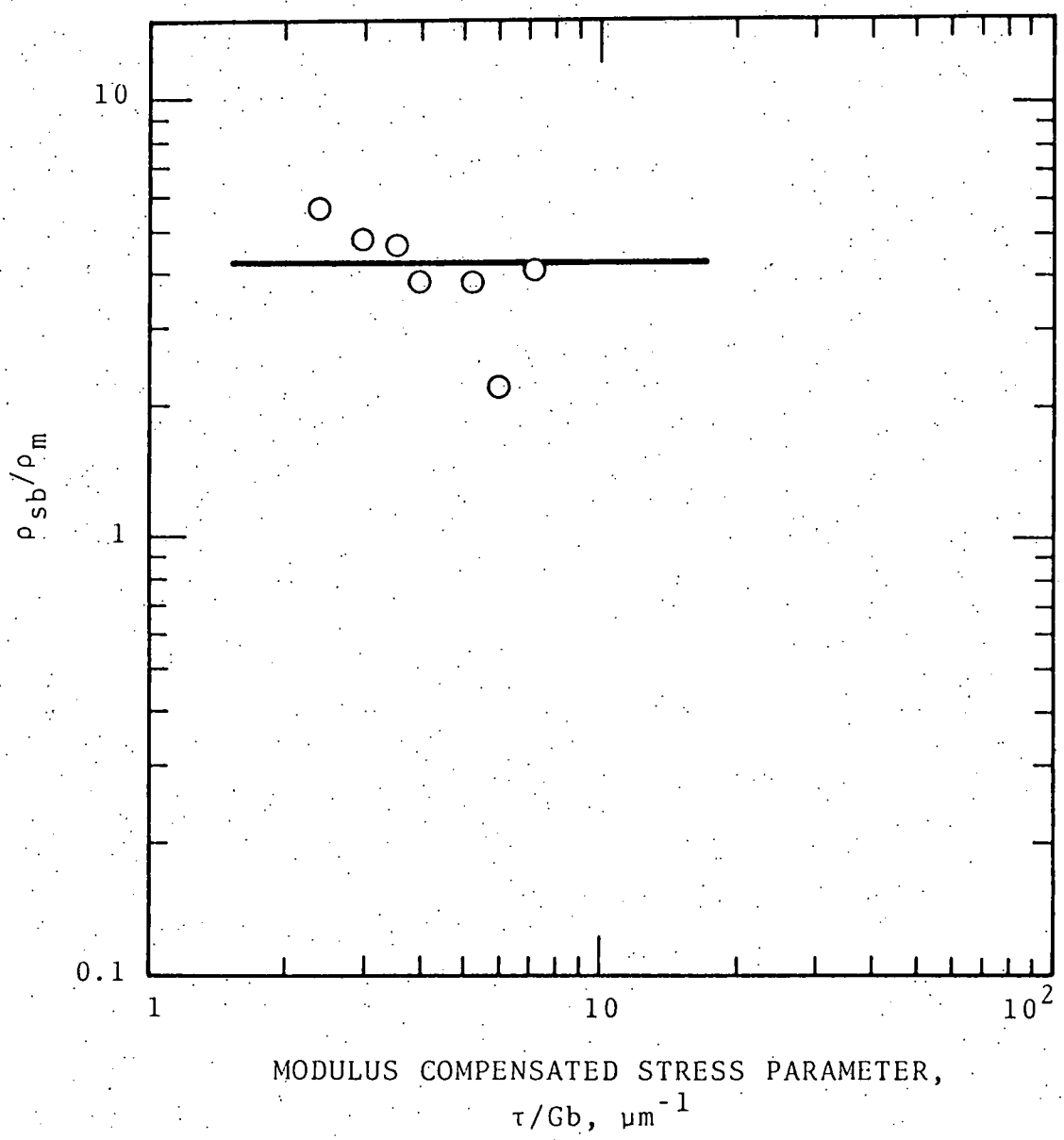

Fig. 1 The Ratio ρ_{sb}/ρ_m in Steady-State and Tertiary State Creep Plotted Against τ/Gb for 316 Stainless Steel.

Fig. 2(a)

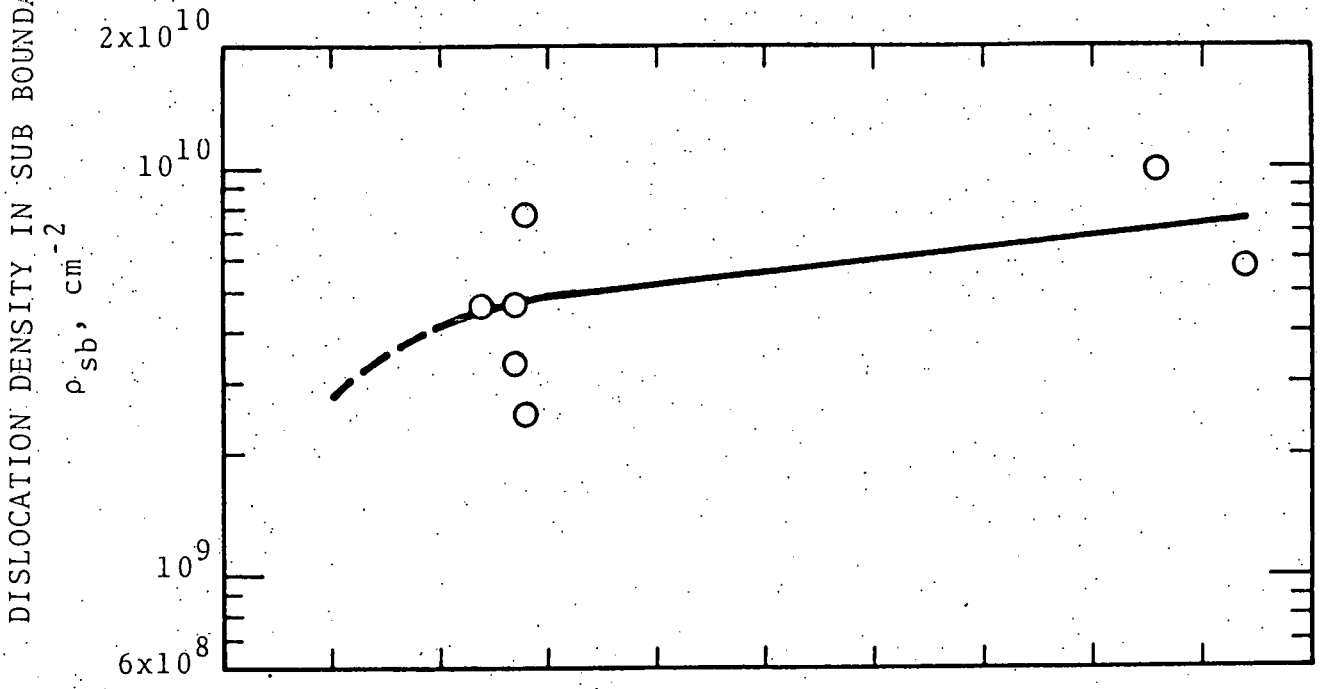

Fig. 2(b)

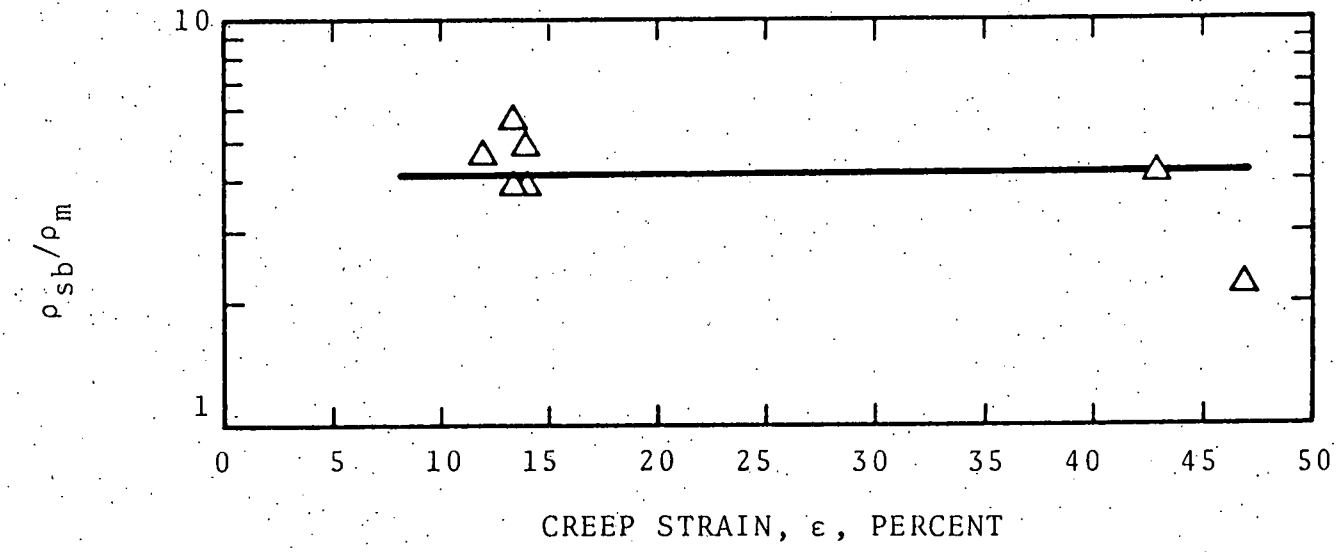

Fig. 2(a) Density of Dislocations Bound in Sub-Boundaries, ρ_{sb}, as a Function of Creep Strain for 316 Stainless Steel.

Fig. 2(b) The Ratio ρ_{sb}/ρ_m in Steady-State and Tertiary State as a Function of Creep Strain for 316 Stainless Steel.

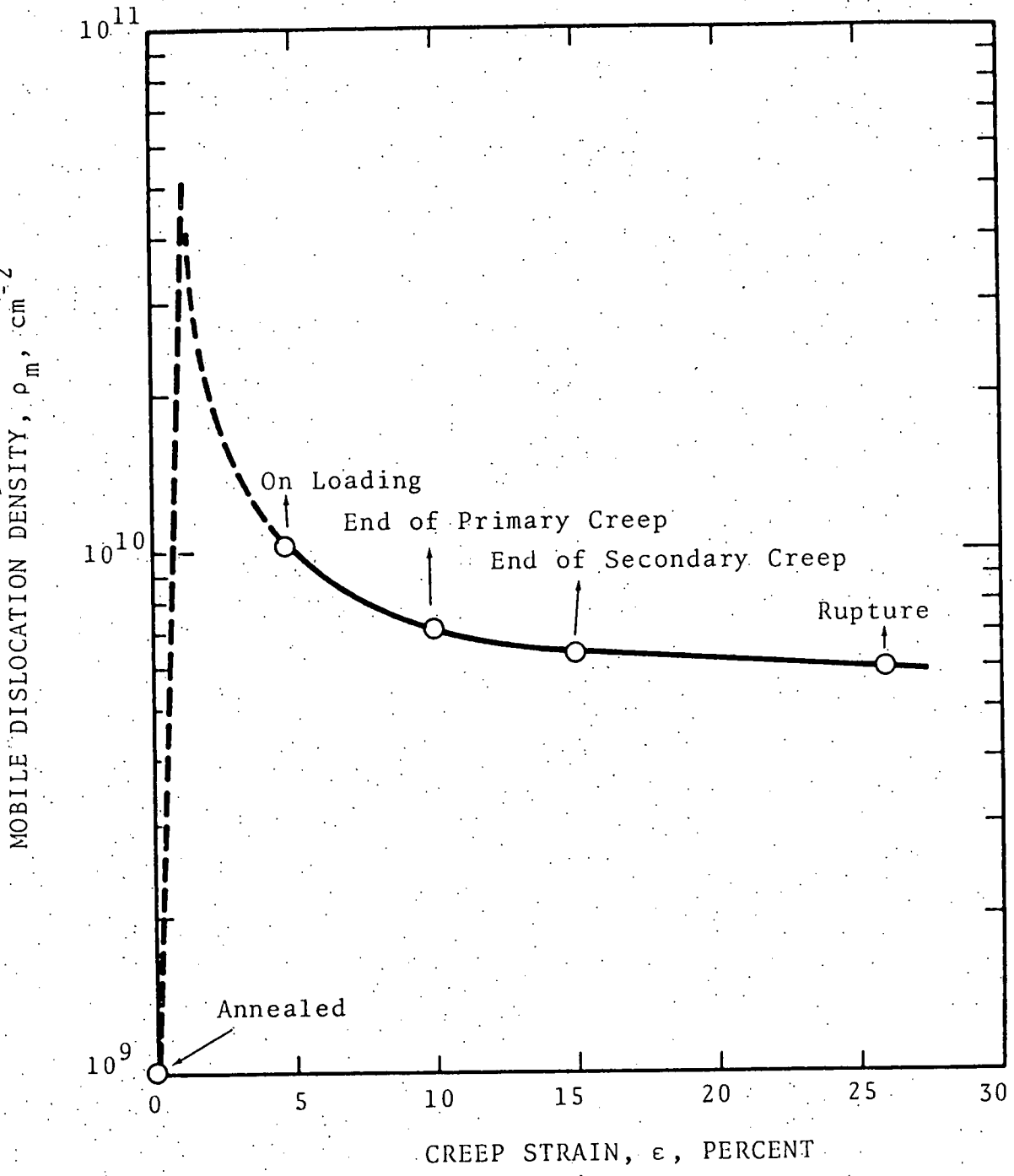

Fig. 3 Mobile Dislocation Density Versus Creep Strain for 304 Stainless Steel Tested at 593°C and at an Applied Stress of 30 Ksi.

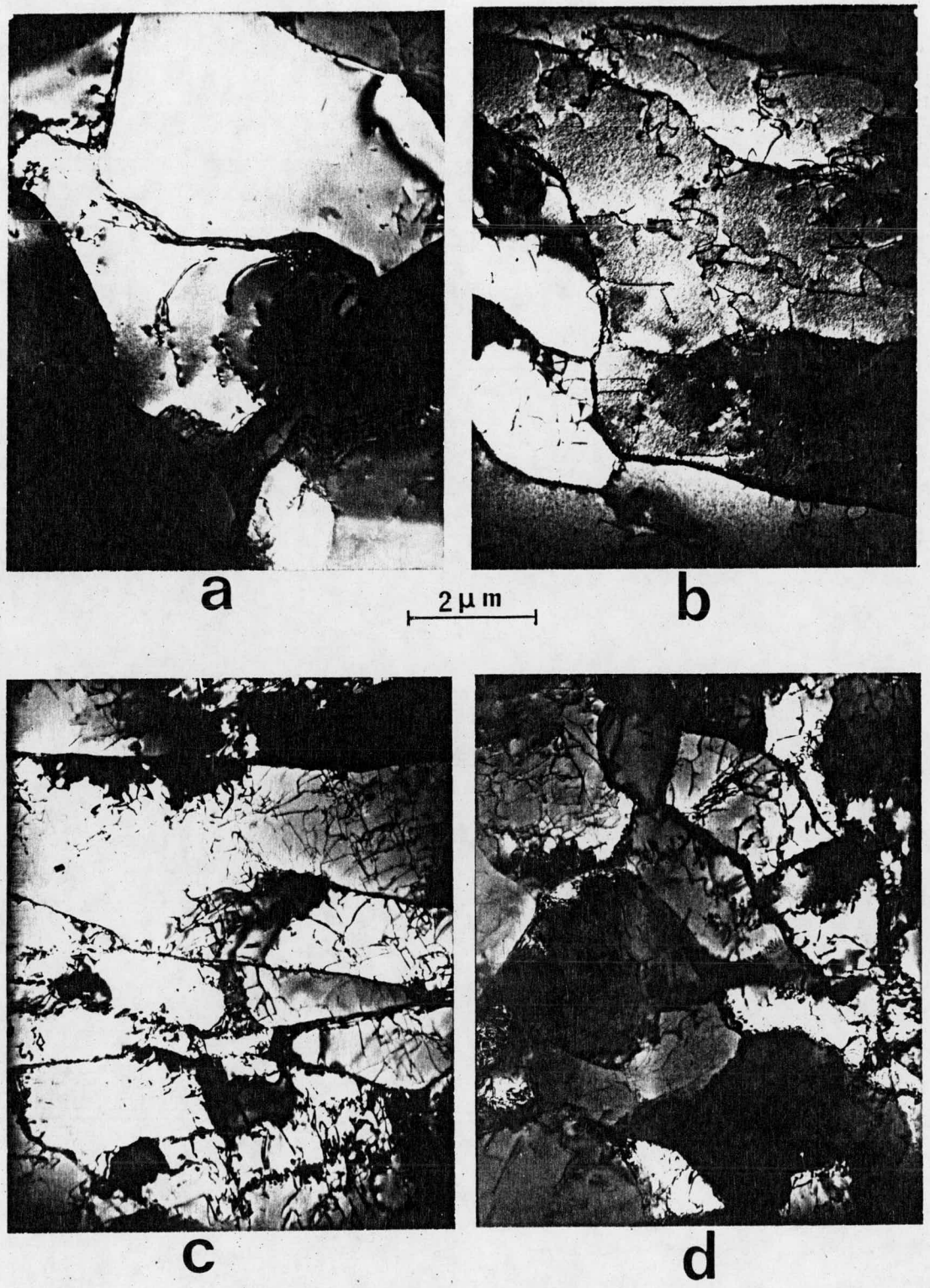

Fig. 4. Typical Substructure Developed in Creep Tested AISI 304 Stainless Steel (Heat 9T2796) at (a) 816°C, 52 MPa, (b) 760°C, 69 MPa, (c) 704°C, 103 MPa, and 760°C, 138 MPa.

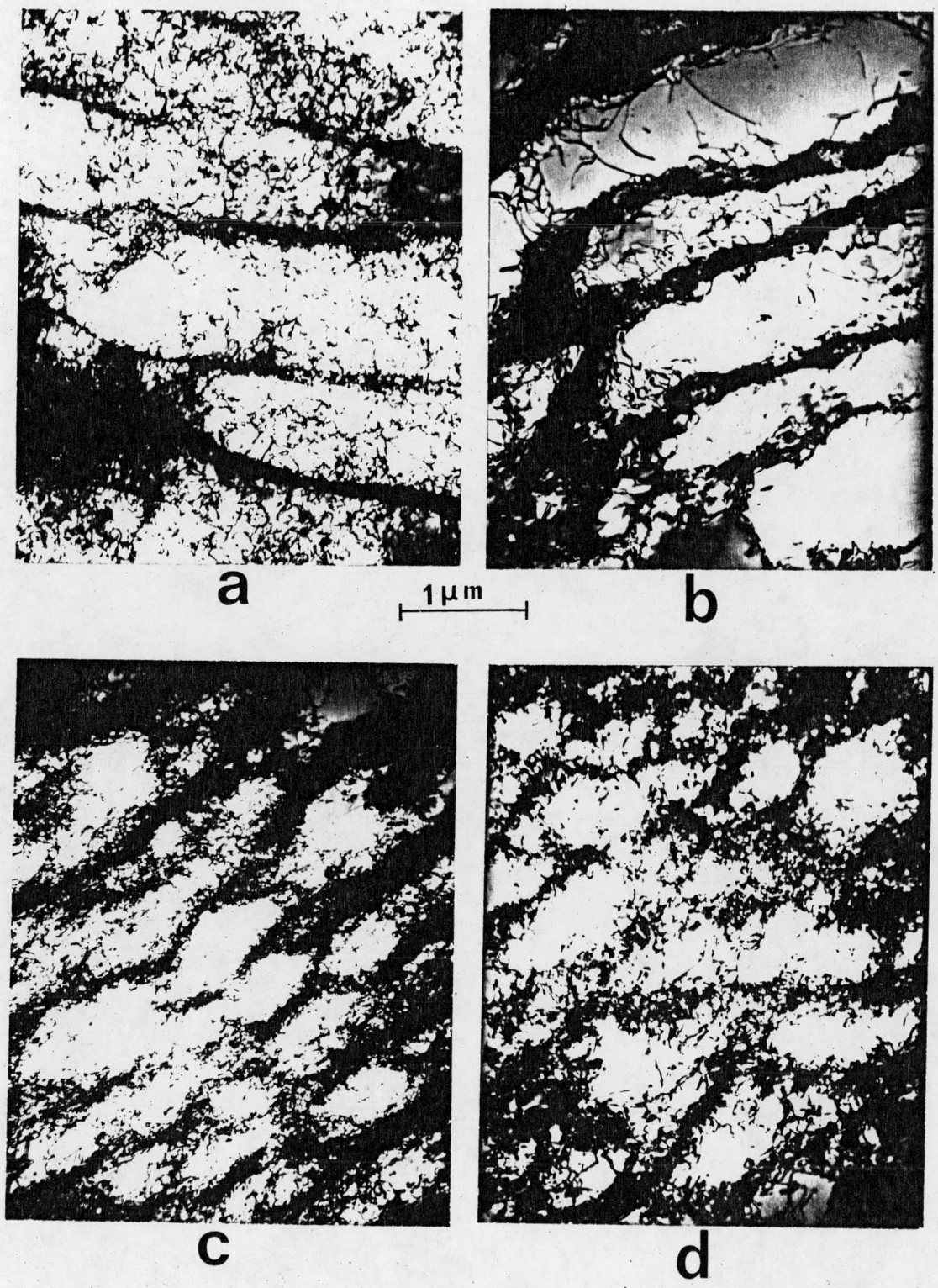

Fig. 5. Typical Substructure Developed in AISI 304 Stainless Steel (Heat 9T2796) (a) 649°C, 172 MPa, creep, (b) 704°C, $\dot{\varepsilon} = 8.3 \times 10^{-5}$ sec^{-1}, tensile, (c) 538°C, 276 MPa, creep and (d) 649°C, $\dot{\varepsilon} = 8.3 \times 10^{-5}$ sec^{-1}, tensile.

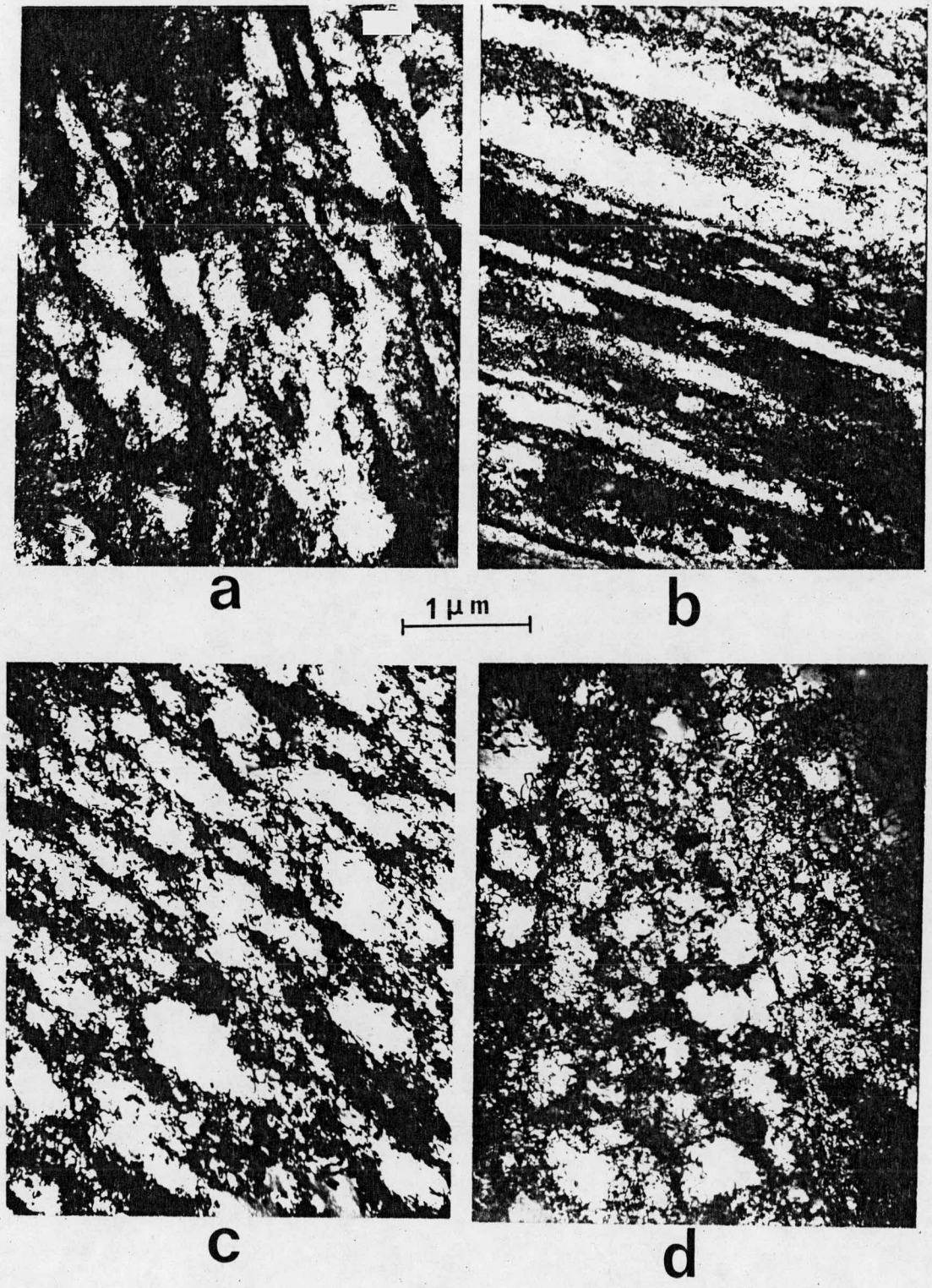

Fig. 6. Typical Substructure Developed in AISI 304 Stainless Steel (Heat 9T2796) Tested in Tension at (a) and (b) 538°C, $\dot{\varepsilon} = 8.3 \times 10^{-5}$ sec^{-1}, (c) 593°C, $\dot{\varepsilon} = 8.3 \times 10^{-5}$ sec^{-1} and (d) 649°C, $\dot{\varepsilon} = 8.3 \times 10^{-4}$ sec^{-1}.

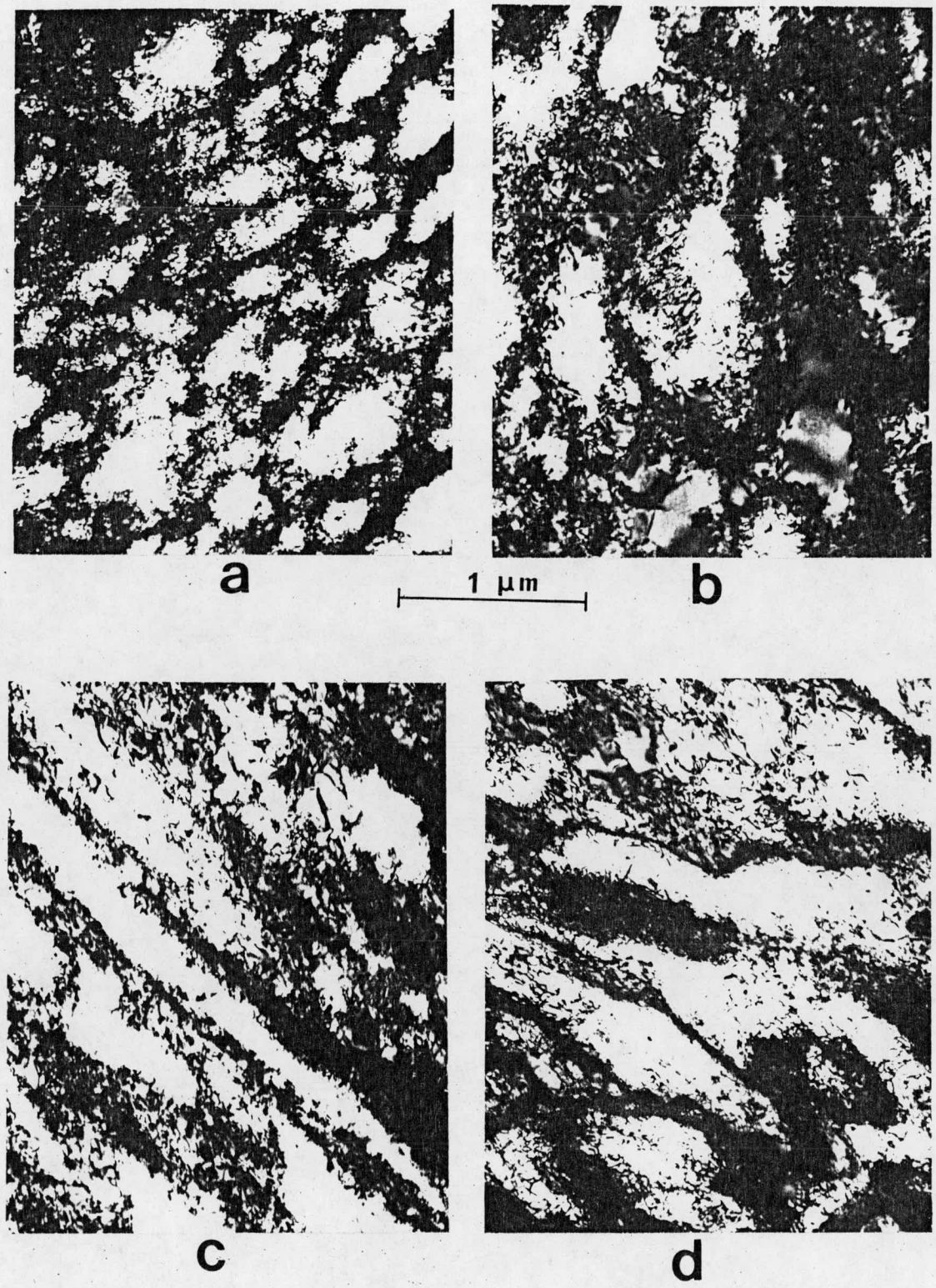

Fig. 7. Typical Substructure Developed in AISI 304 Stainless Steel (Heat 9T2796) Tested in Tension at a Strain Rate $\dot{\varepsilon} = 8.3 \times 10^{-2}$ sec^{-1} at (a) 538°C, (b) 593°C, (c) 649°C and (d) 704°C.

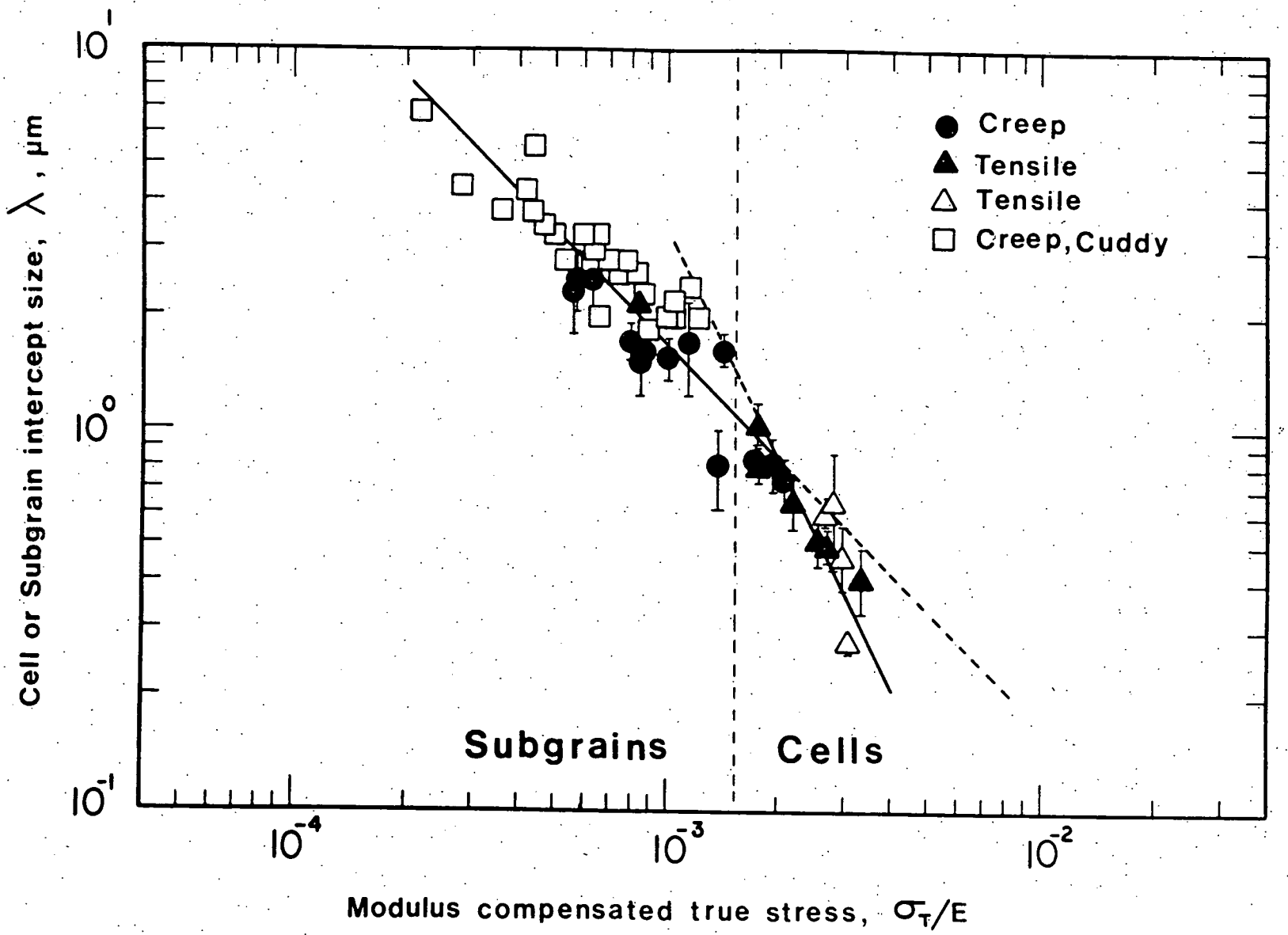

Fig. 8. Plot of the Cell of Subgrain Intercept Size, λ, vs. the Modulus Compensated True Stress, σ_T/G on a log-log Scale (AISI 304 Stainless Steel).

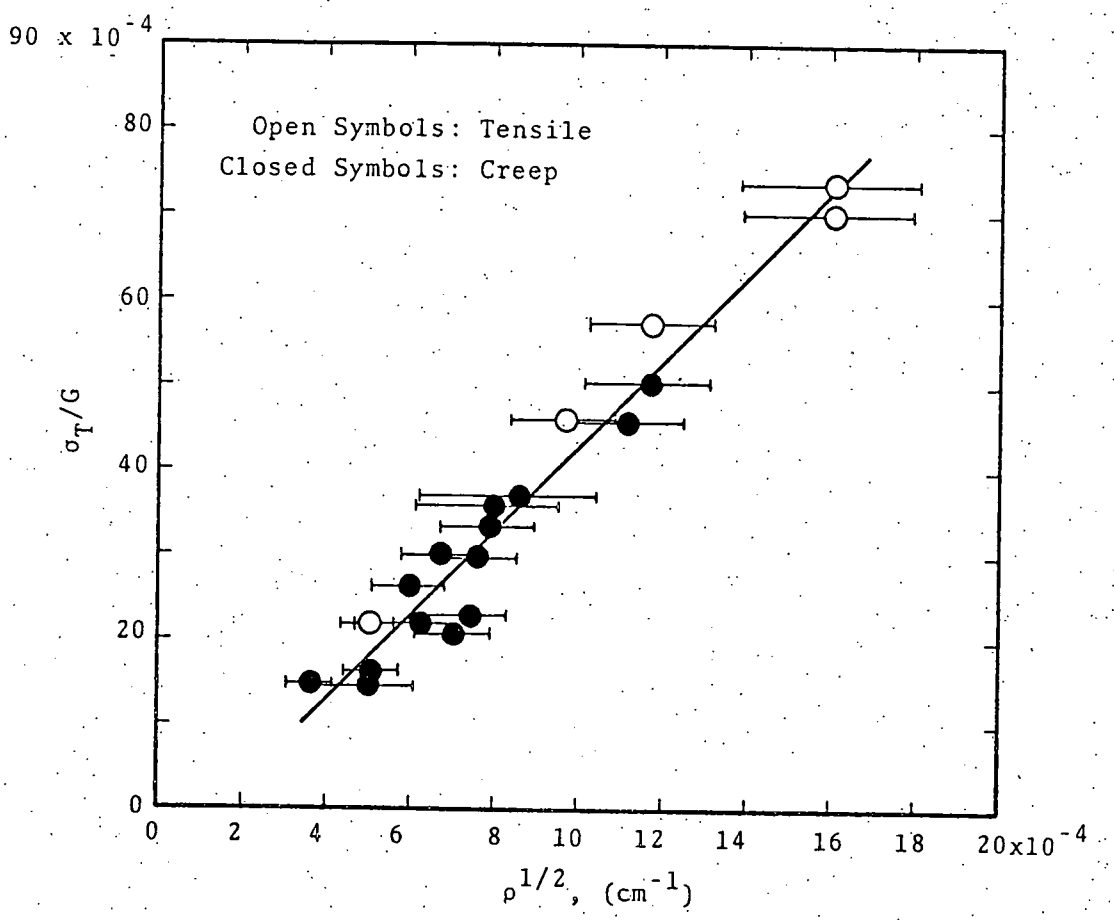

Fig. 9. Plot of the Modulus Compensated True Stress, σ_T/G, vs. the Square Root of the Dislocation Density, $\rho^{1/2}$, AISI 304 SS, (Reference Heat 9T2796).

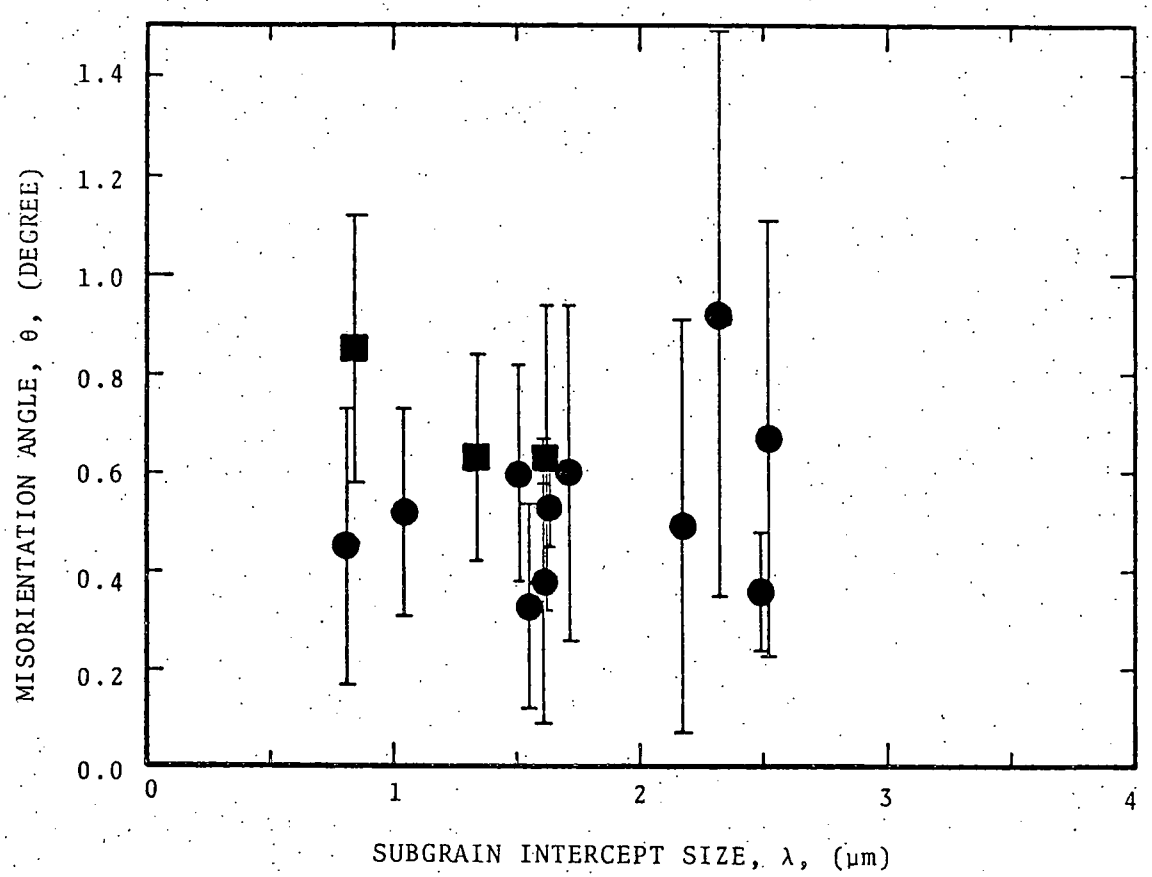

Fig. 10. Plot of the Misorientation Angle, θ, vs. the Subgrain Intercept Size, λ (AISI 304 SS).

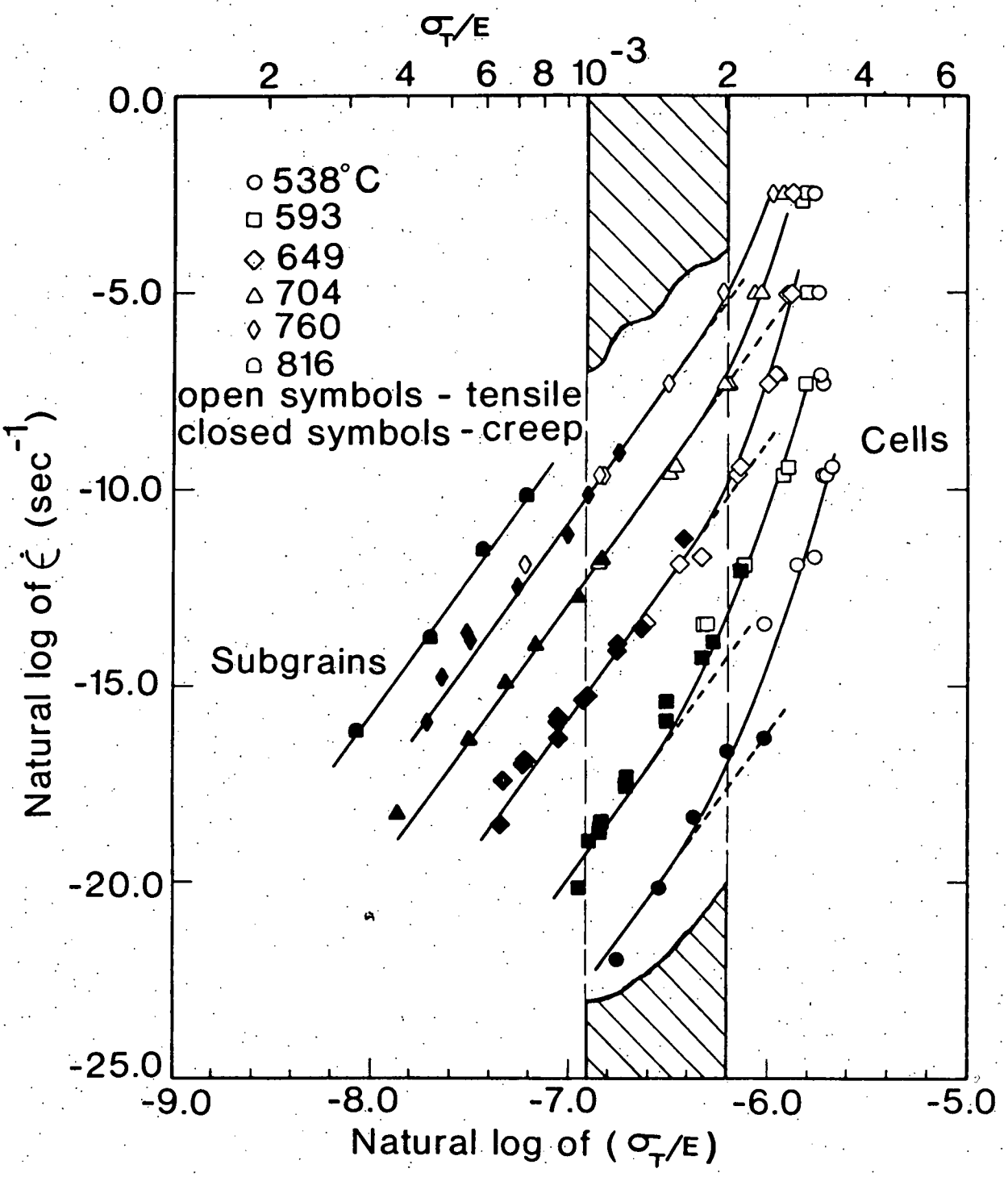

Fig. 11-A. Plot of the Natural Log of the Deformation Rate, $\dot{\epsilon}$, vs. the Natural Log of the Modulus Compensated Stress, σ_T/E. (AISI 304 Stainless Steel, Reference Heat 9T2796).

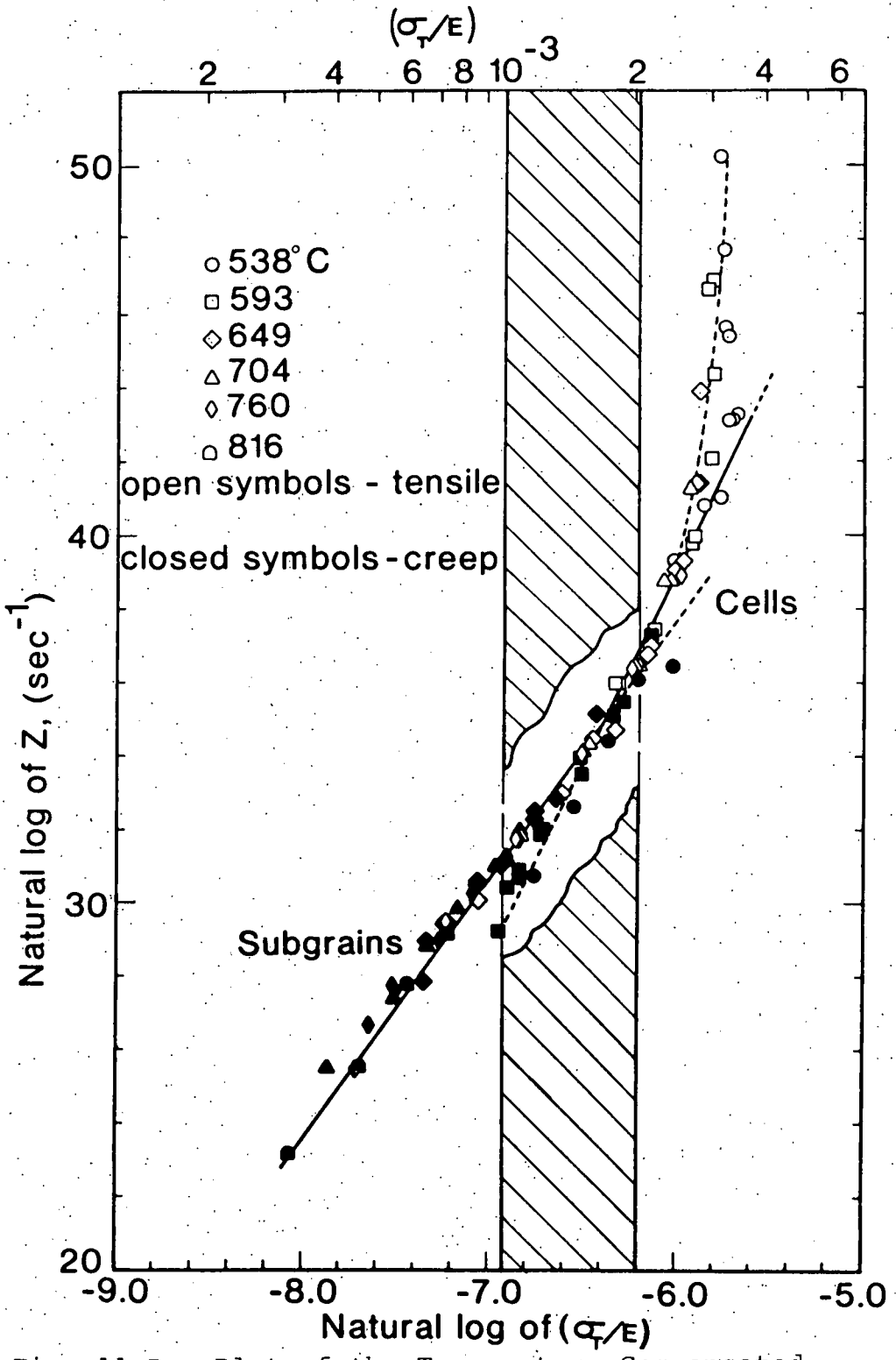

Fig. 11-B. Plot of the Temperature Compensated Deformation Rate, Z, vs. the Modulus Compensated Stress, σ_T/E, on a ℓn-ℓn Scale. (AISI 304 Stainless Steel, Reference Heat 9T2796).

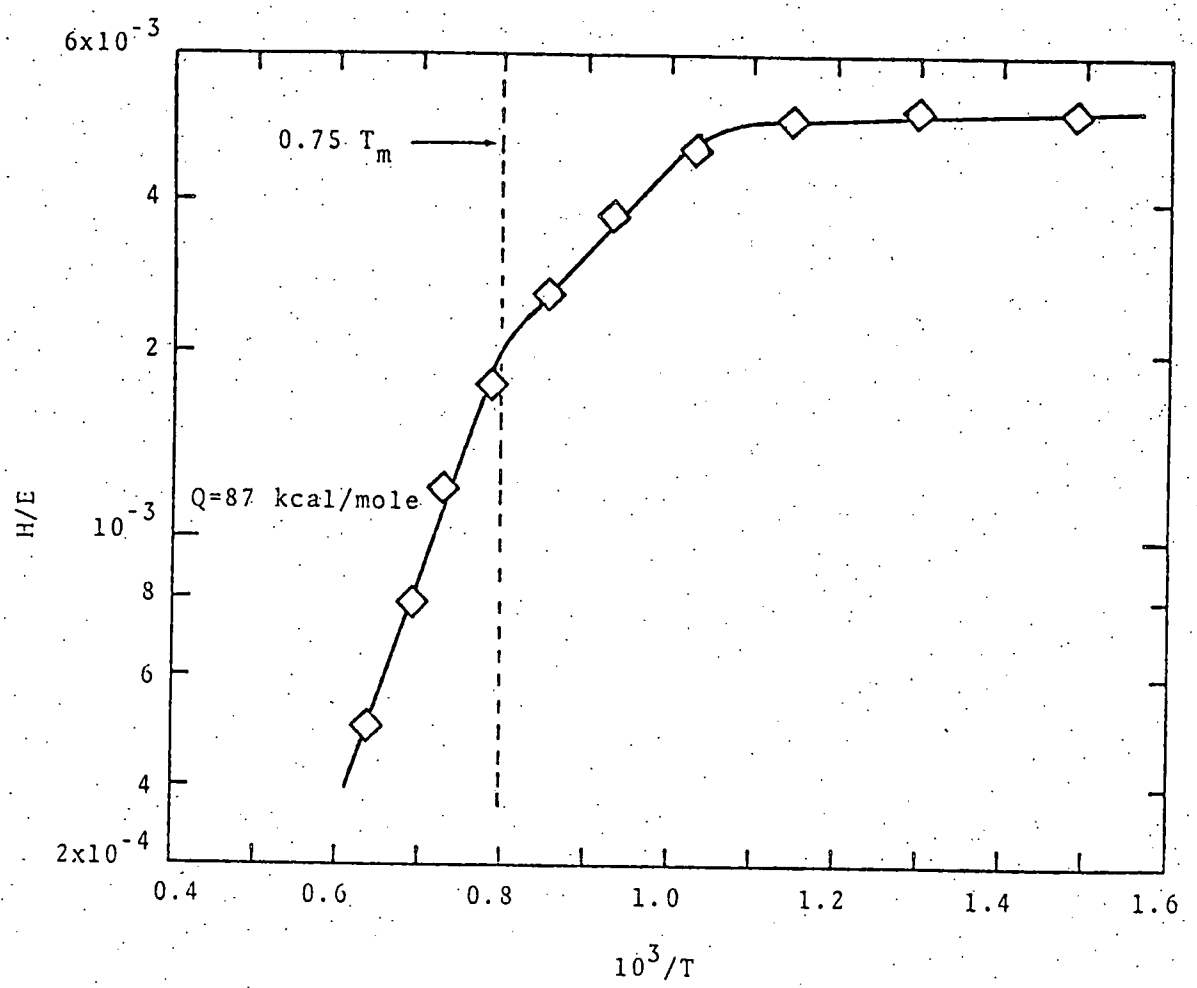

Fig. 12. Plot of Hardness/Young's Modulus Ratio as a Function of Reciprocal Temperature for 304 Stainless Steel, Heat Number 9T2796.

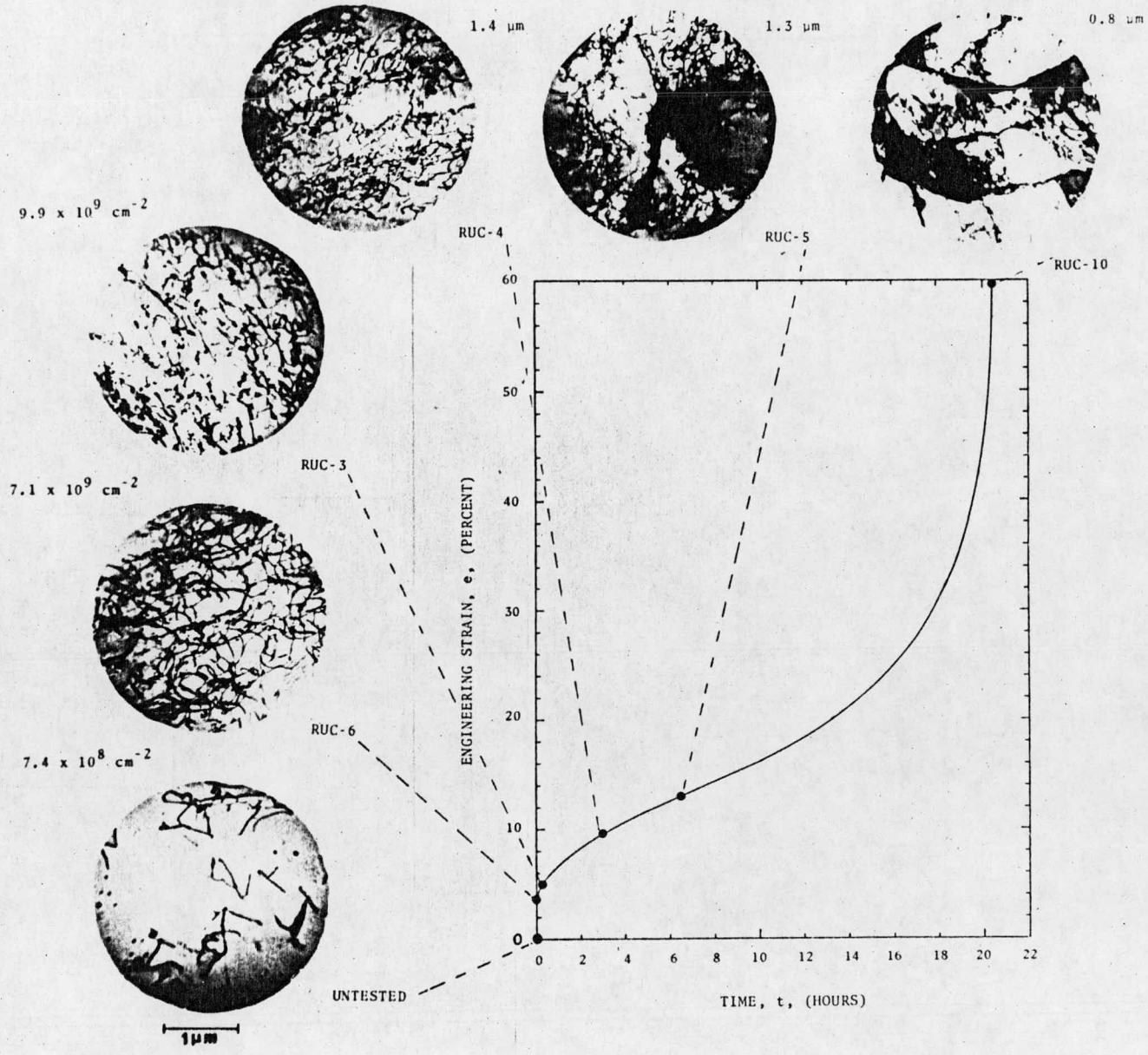

Fig. 13. Strain Behavior in 304 SS as a Function of Time During Creep at 704°C with Corresponding Dislocation Substructures. (Stress 17.58 $kg \cdot mm^{-2}$).

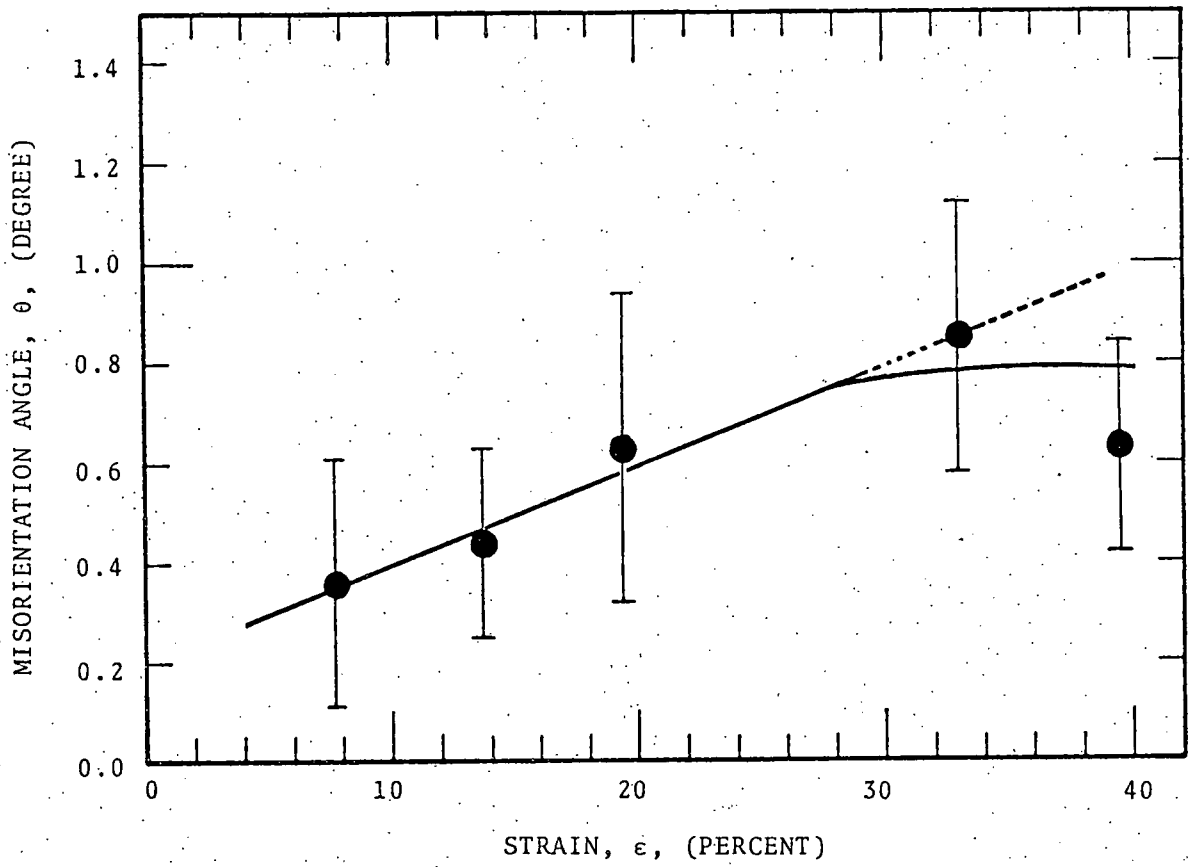

Fig. 14. Plot of the Misorientation Angle, θ, vs. the Strain, ε, of AISI 304 SS (Heat G8607) Creep Tested at 704°C.

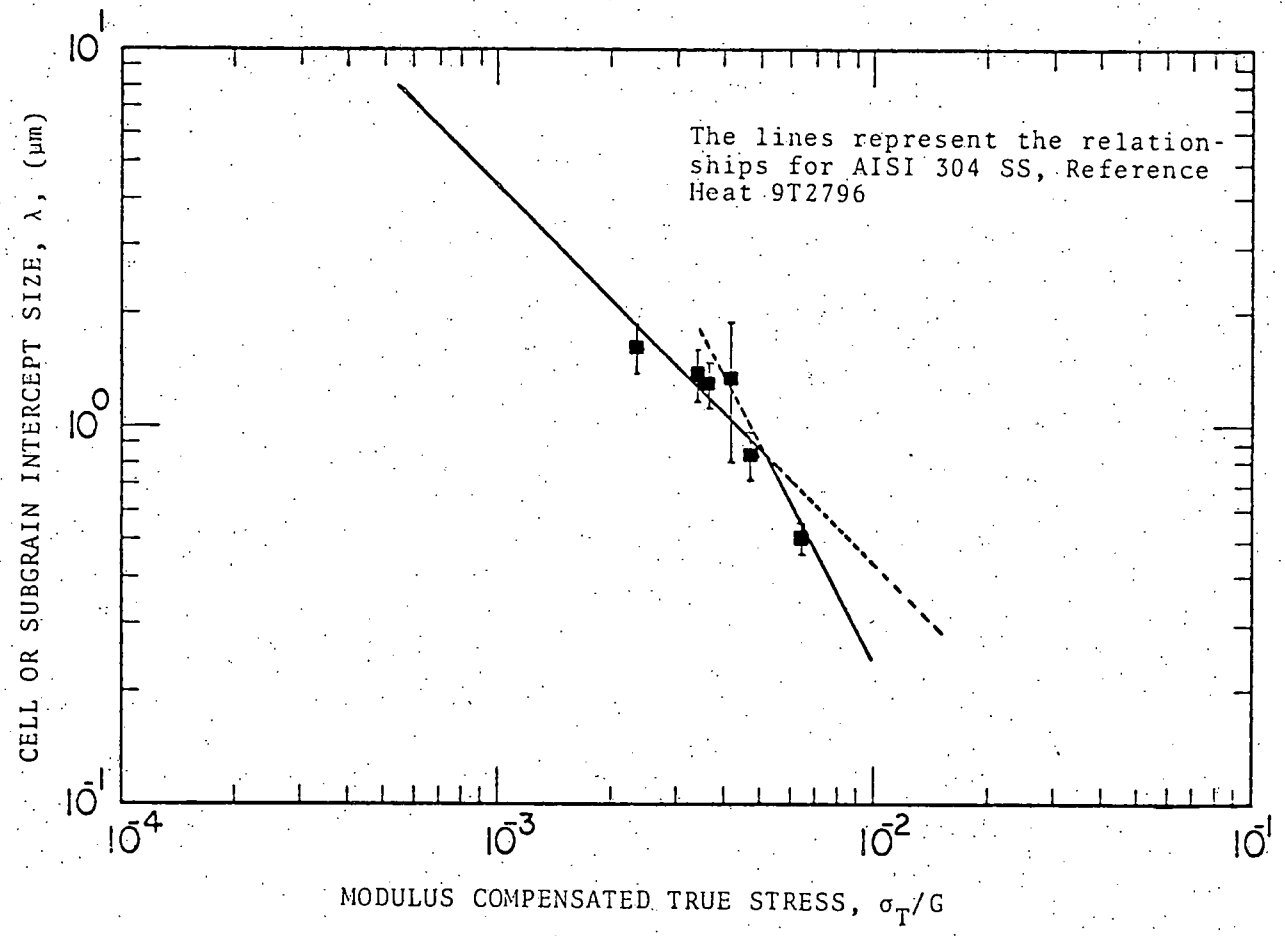

Fig. 15. Plot of the Cell or Subgrain Intercept Size, λ, vs. the Modulus Compensated True Stress, σ_T/G (AISI 304 SS, Heat G8607).

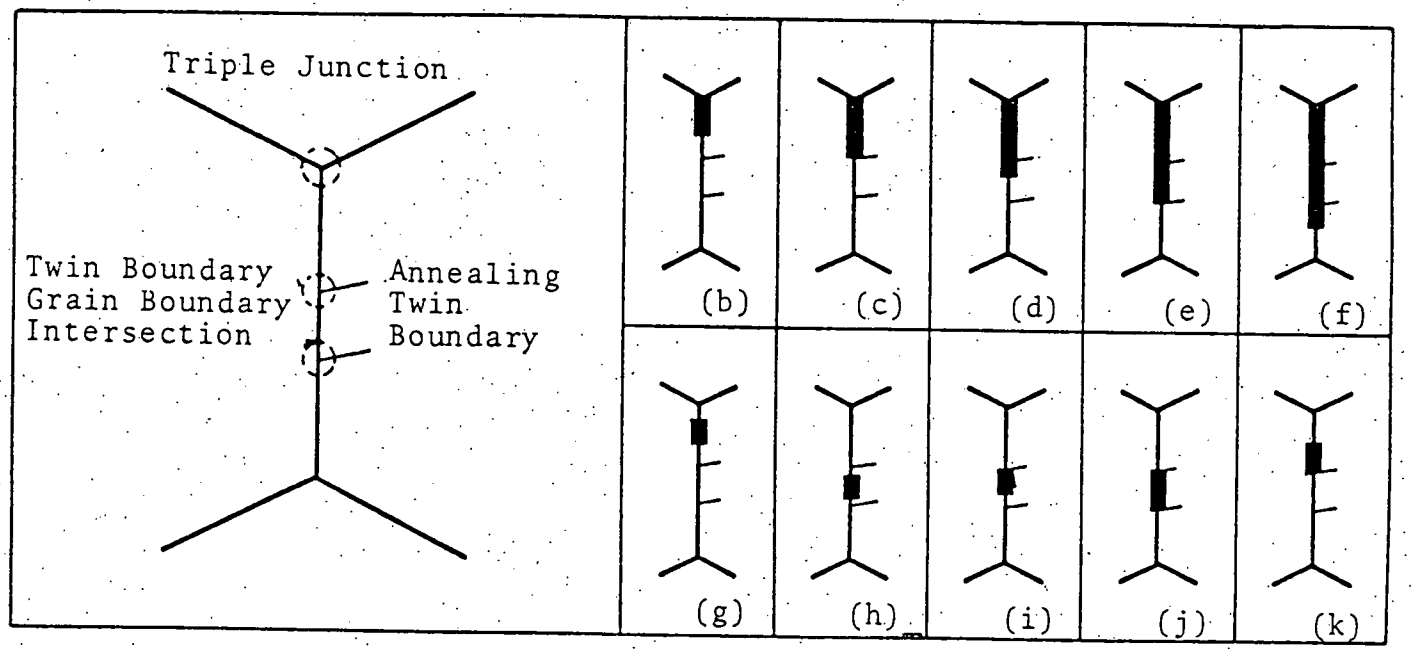

Fig. 16. Schematics Showing Various Types of Cracks

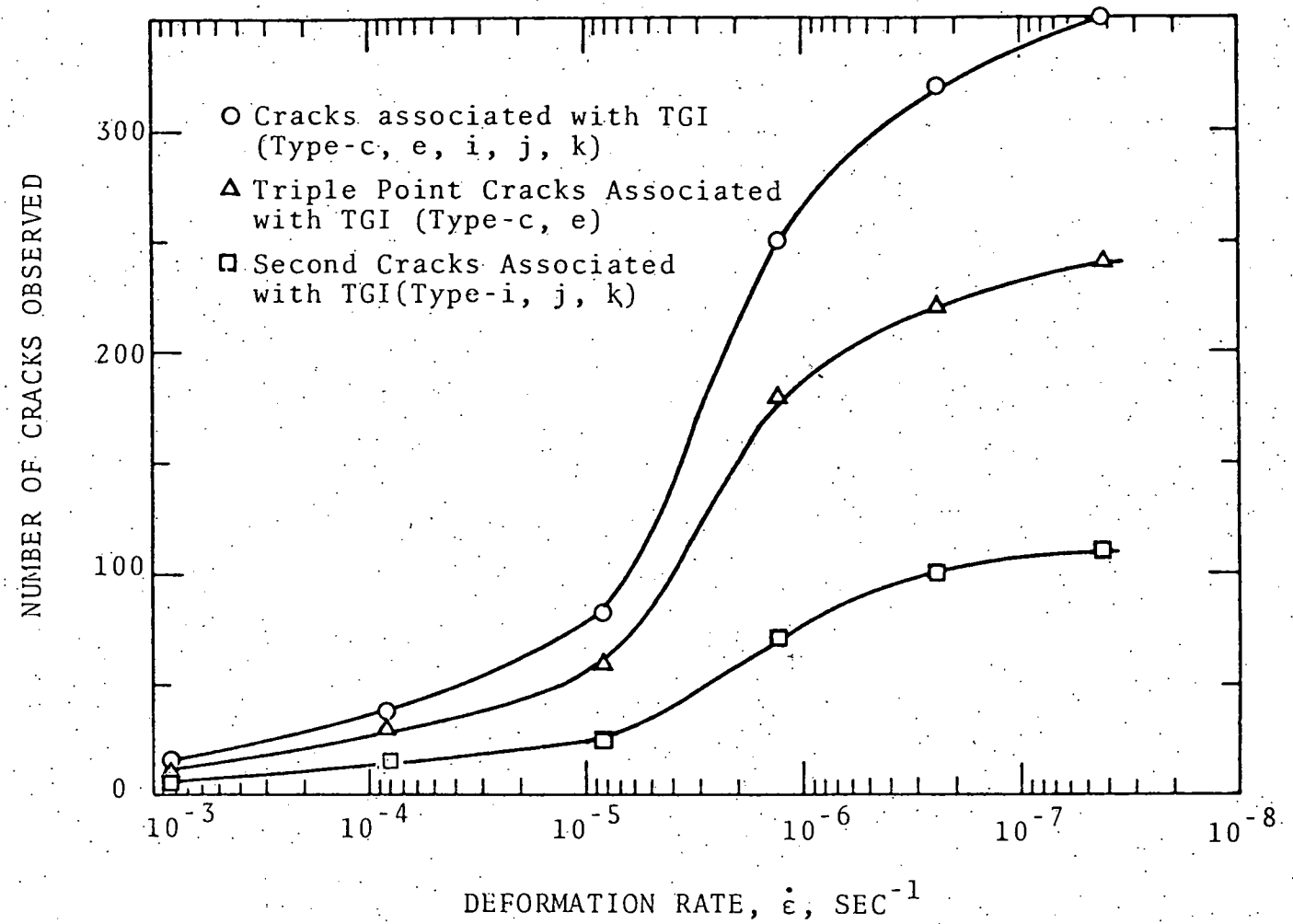

Fig. 17. Distribution of Intergranular Cracks Associated With Twin Boundary - Grain Boundary Intersection (TGI) as a Function of Deformation Rate.

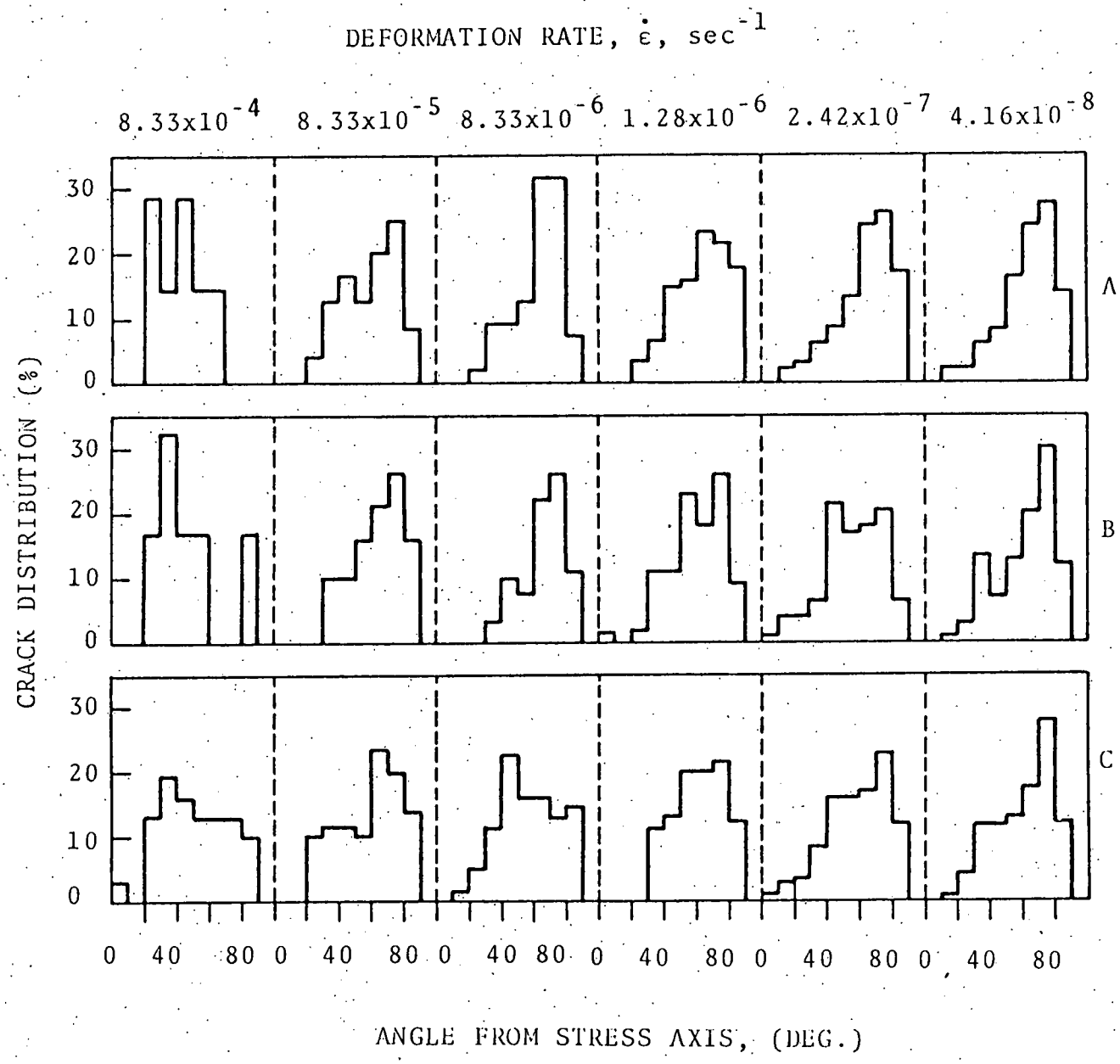

Fig. 18. Angular Percentage Distribution of Different Types of Intergranular Cracks: (A) Type c and e; (B) Type i, j and k; (C) Type g to k in Reference to Fig. 16

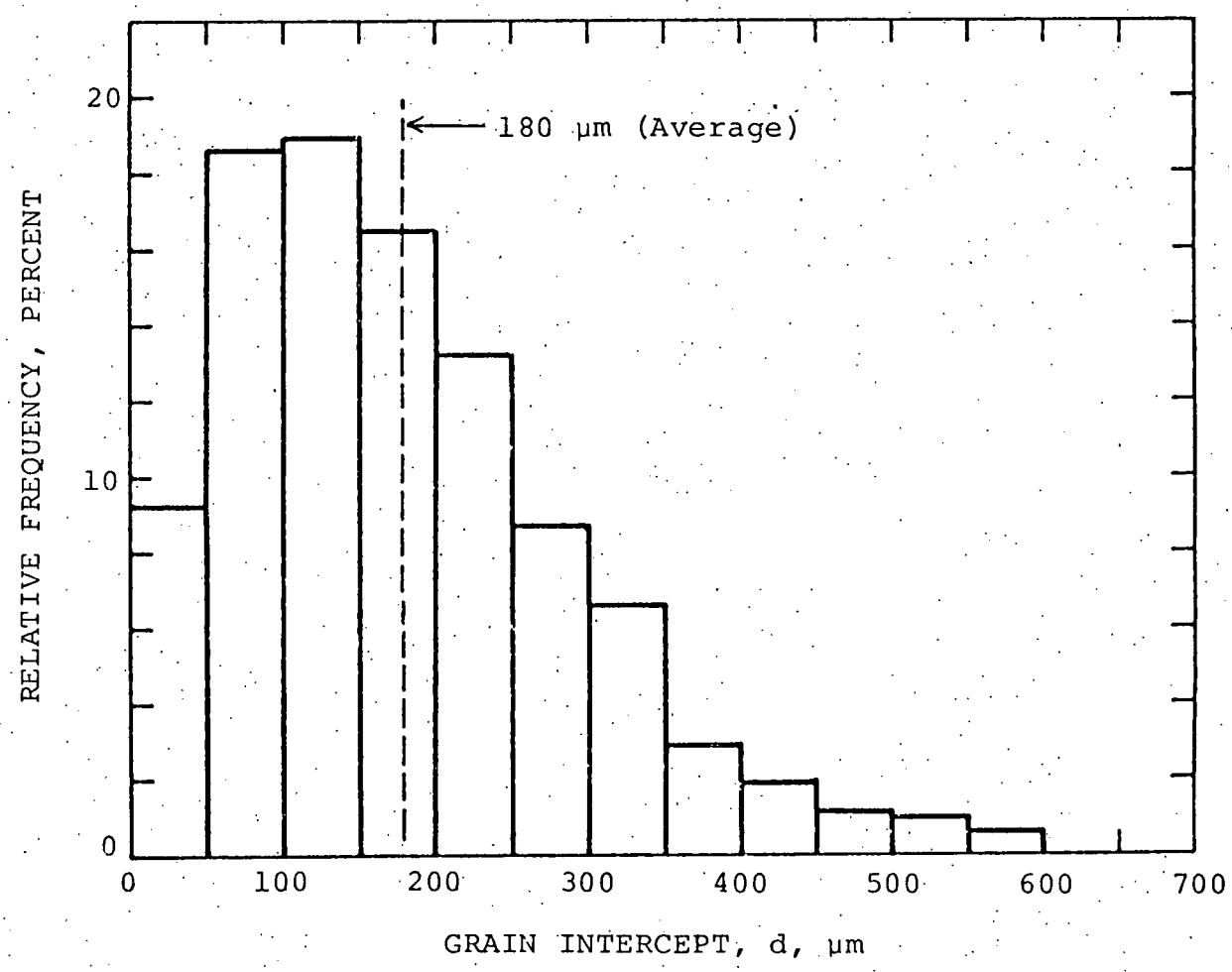

Figure 19. Distribution of Grain Intercepts in the Undeformed Region of a Tensile Tested Specimen ($\dot{\varepsilon}_t = 8.33 \times 10^{-4}$ sec^{-1}) of AISI 304 (9T2796).

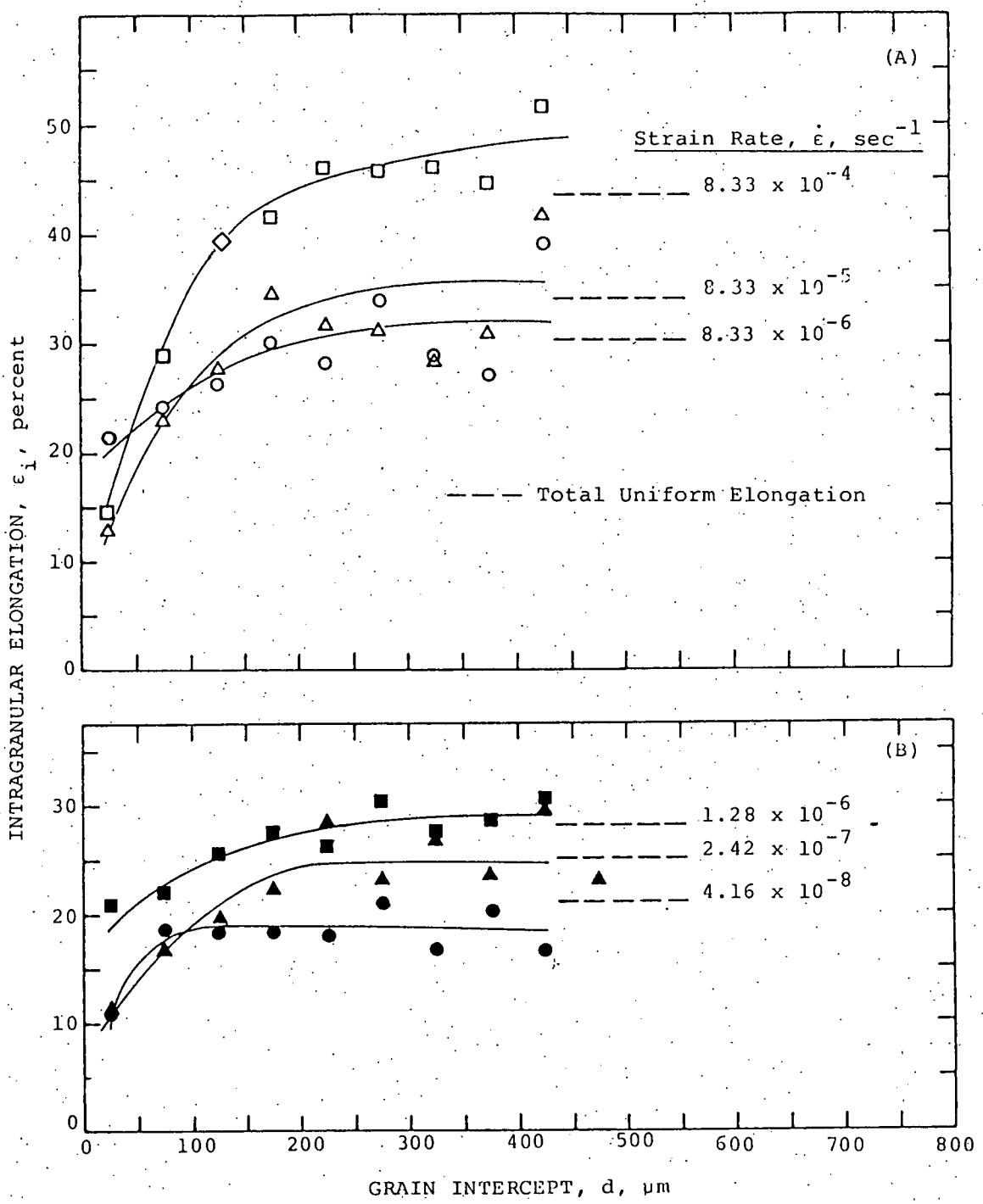

Figure 20. Intragranular Elongation as a Function of Grain Intercept for the Family of Tensile (A) and Creep (B) Tested Specimens of AISI 304 (9T2796) at 650°C.

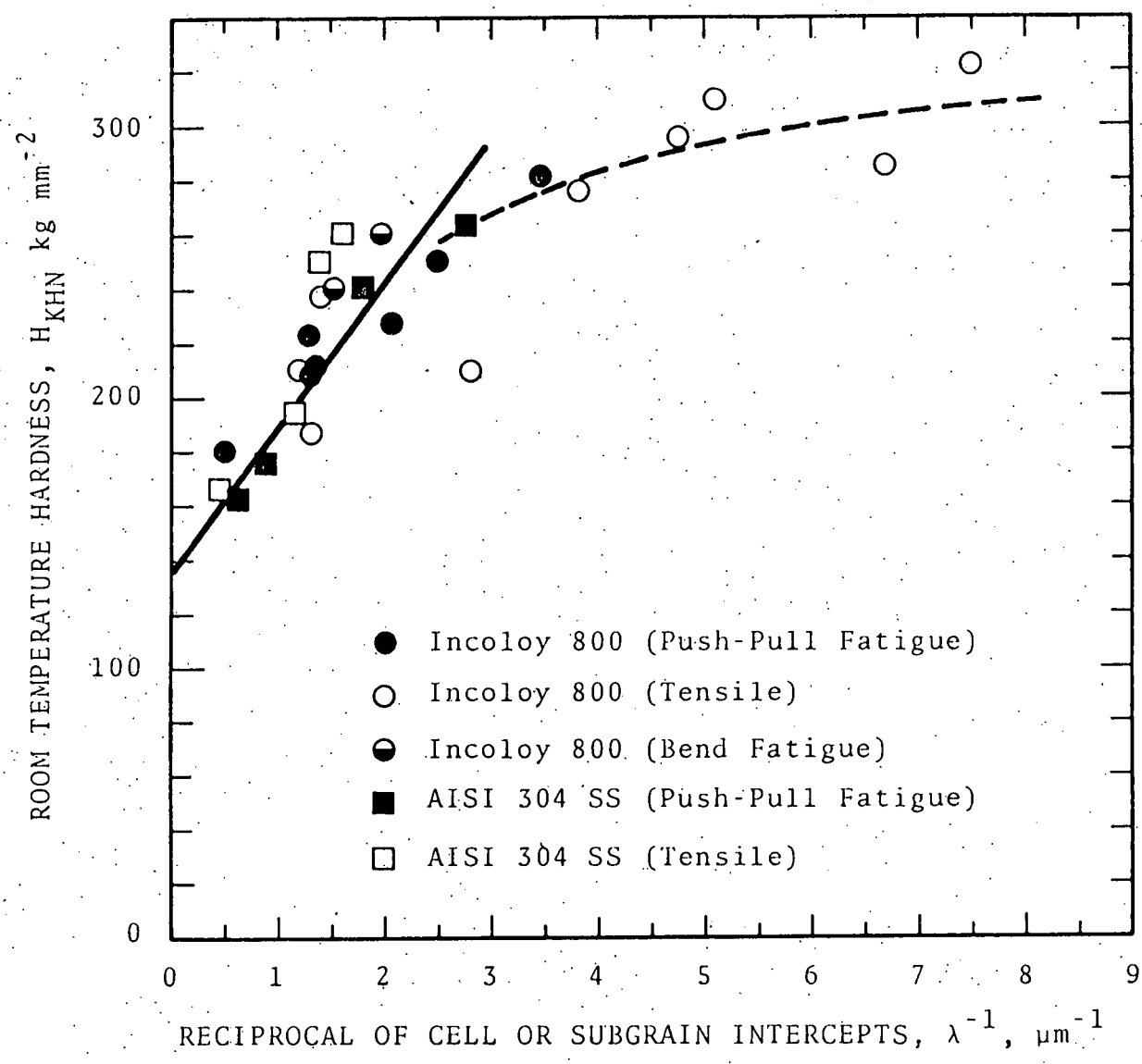

Fig. 21. Room Temperature Hardness as a Function of Reciprocal of Cell or Subgrain Intercepts.

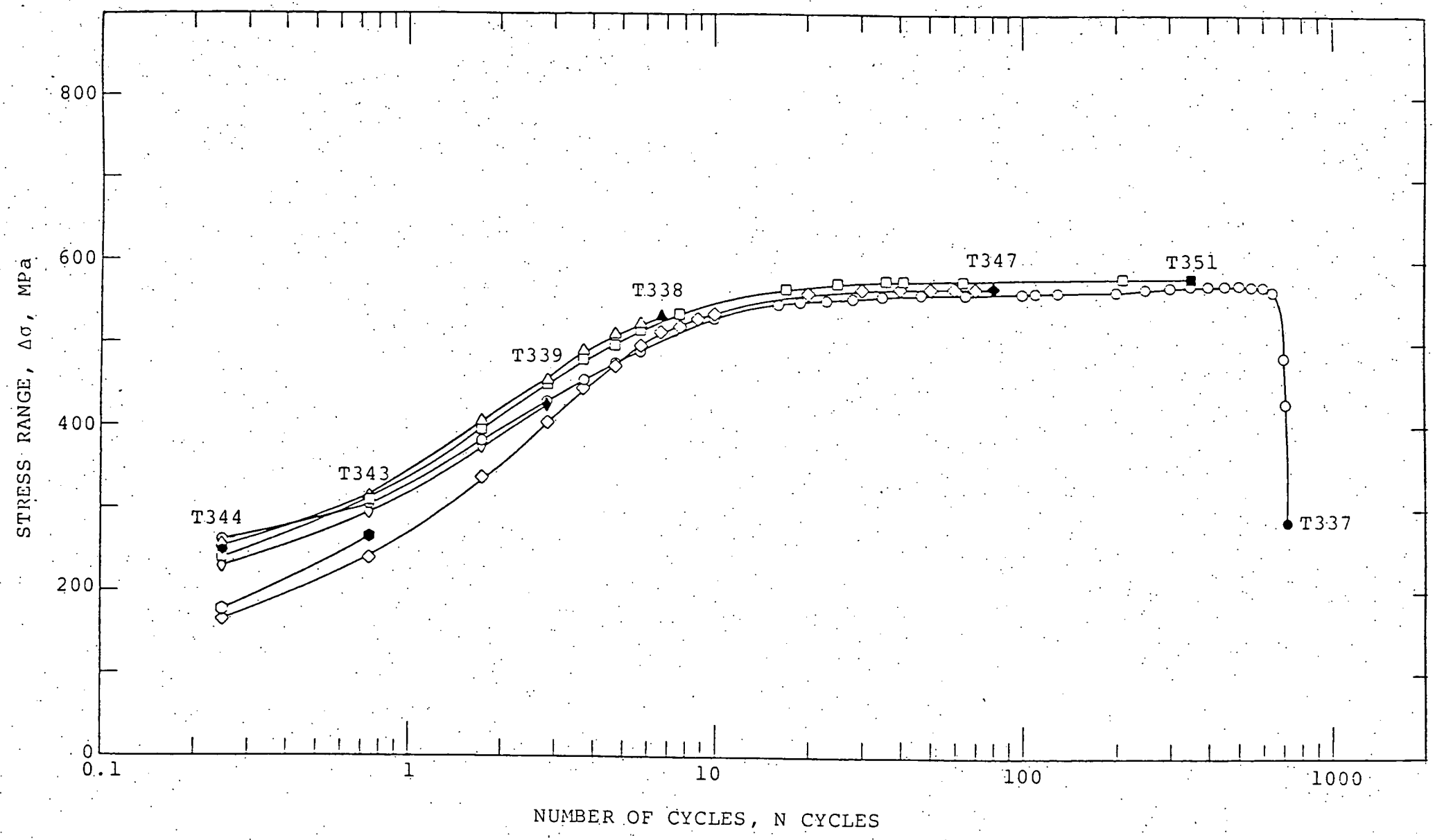

Figure 22. Plot of the Total Stress Range, Δσ, Versus the Number of Cycles, N, for AISI 304 Stainless Steel at 649°C.

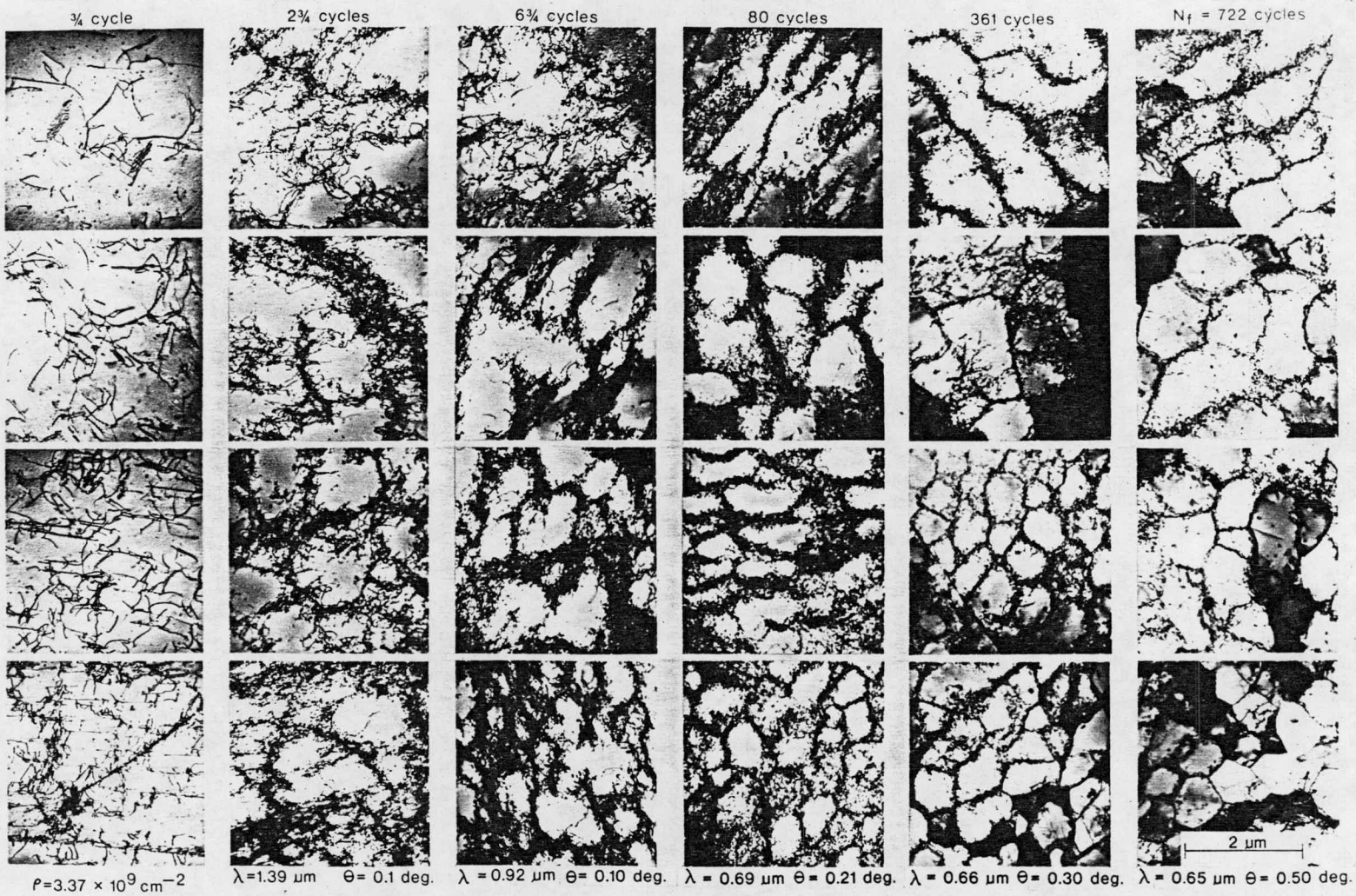

Fig. 23. Low Cycle Fatigue Substructure Development in AISI 304 Stainless Steel at 649°C.

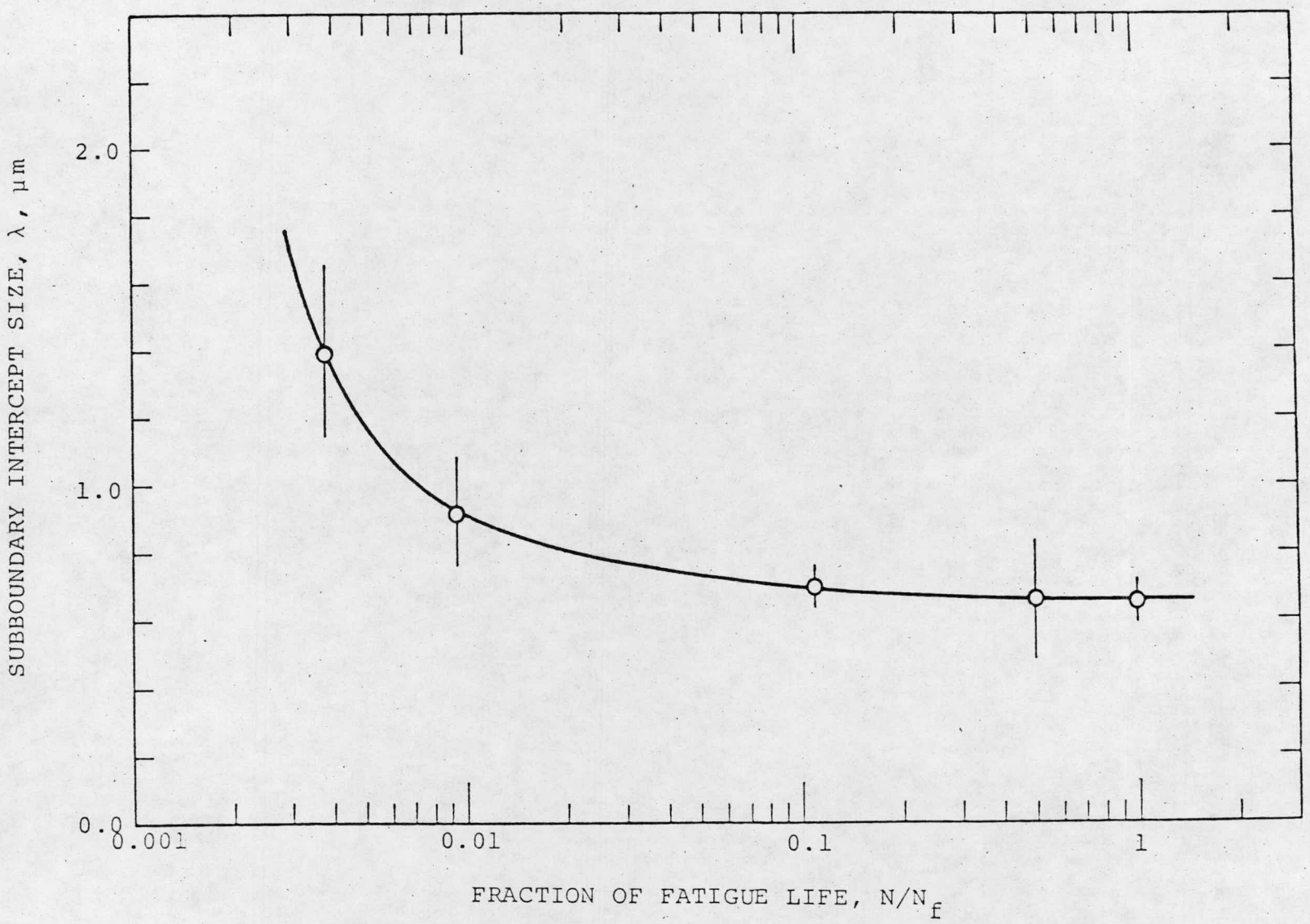

Figure 24. Plot of the Subboundary Intercept Size, λ, Versus the Fraction of Fatigue Life, N/N_f for AISI 304 Stainless Steel at 649°C.

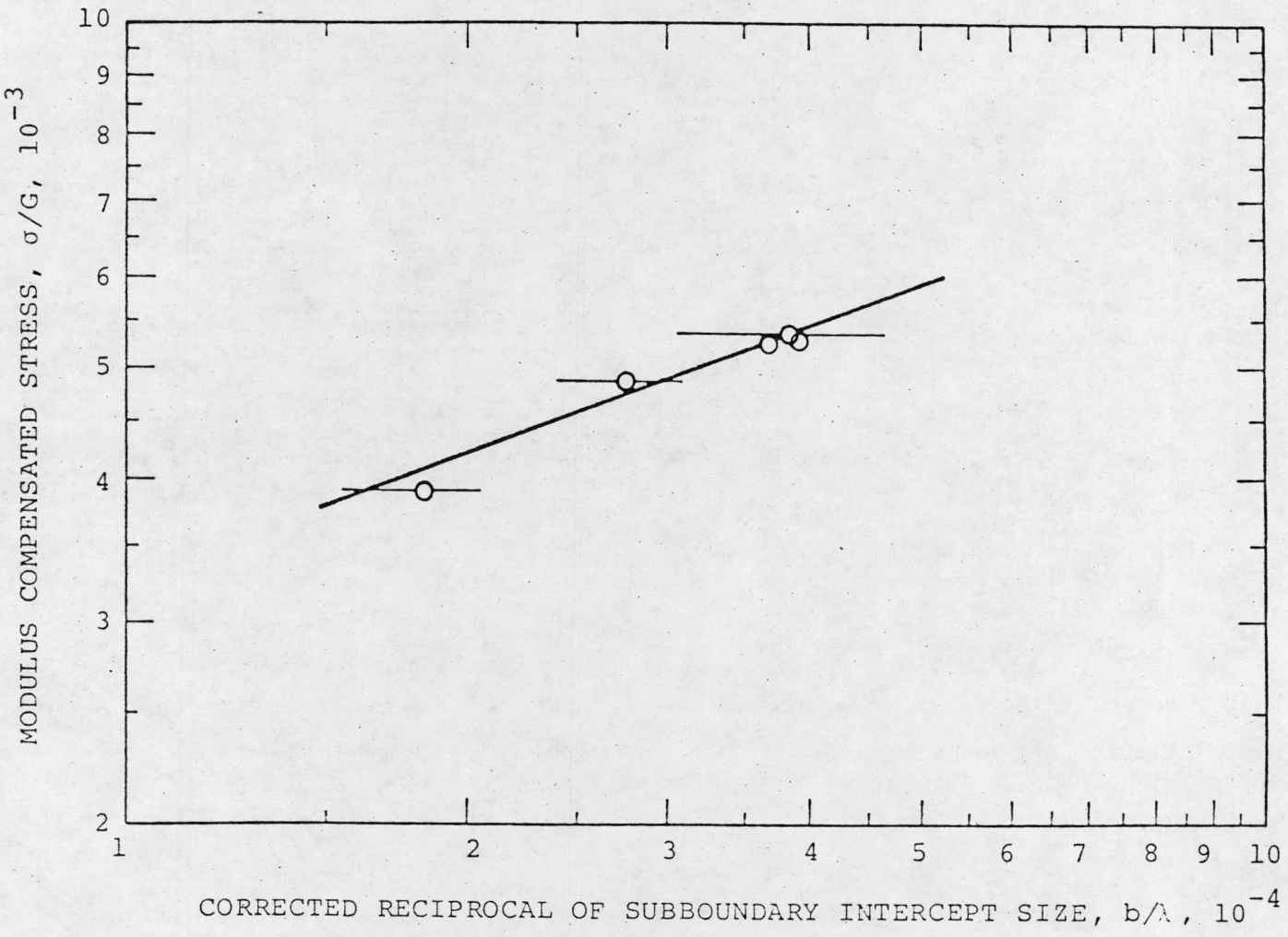

Figure 25. The Shear Modulus Compensated Cyclic Stress Amplitude, σ/G, as a Function of the Corrected Reciprocal of the Subboundary Intercept Size, b/λ, for AISI 304 Stainless Steel at 649°C.

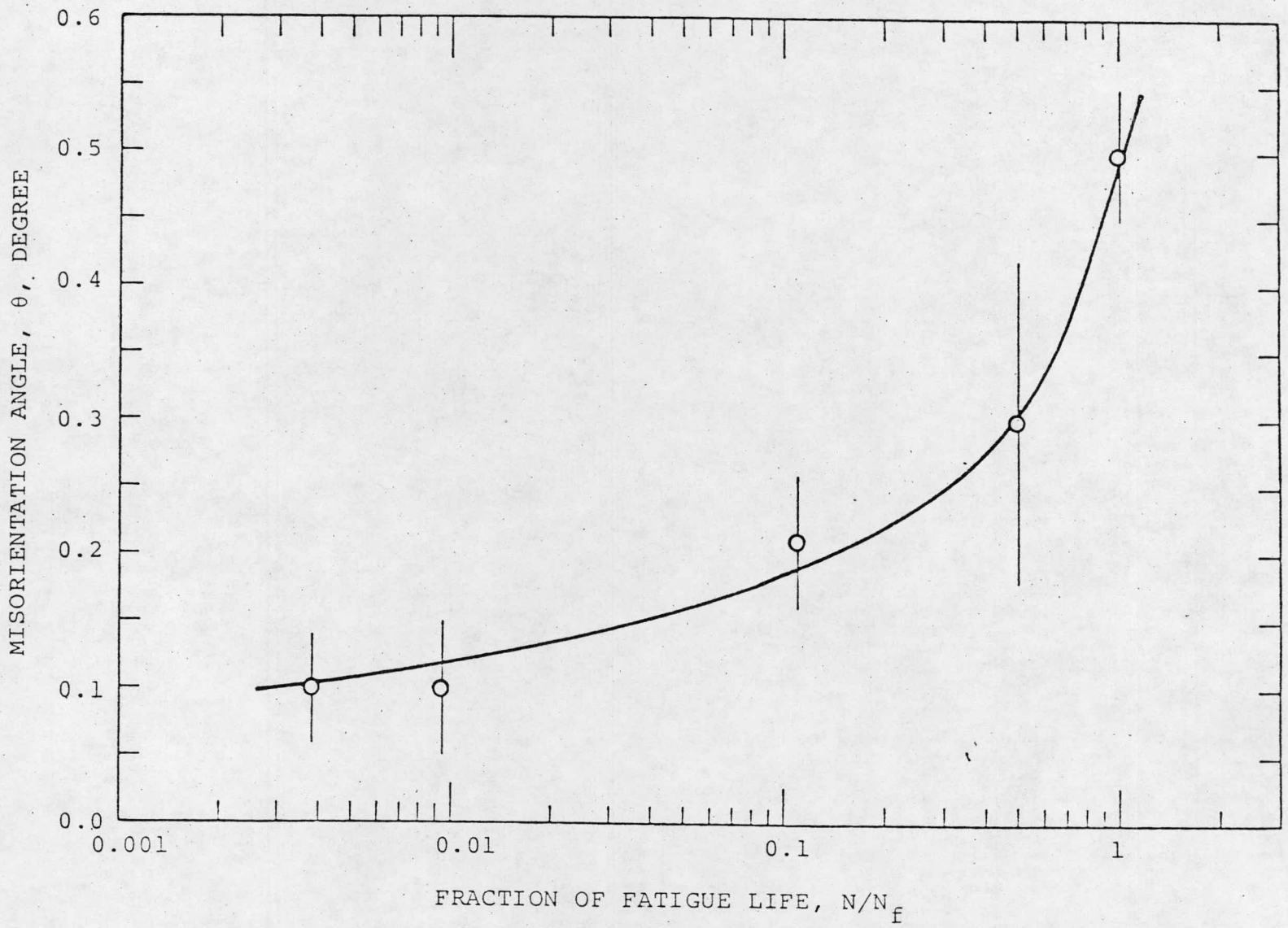

Figure 26. Plot of the Misorientation Angles Between Adjacent Cells, θ, Against the Fraction of Fatigue Life, N/N_f, for AISI 304 Stainless Steel at 649°C.

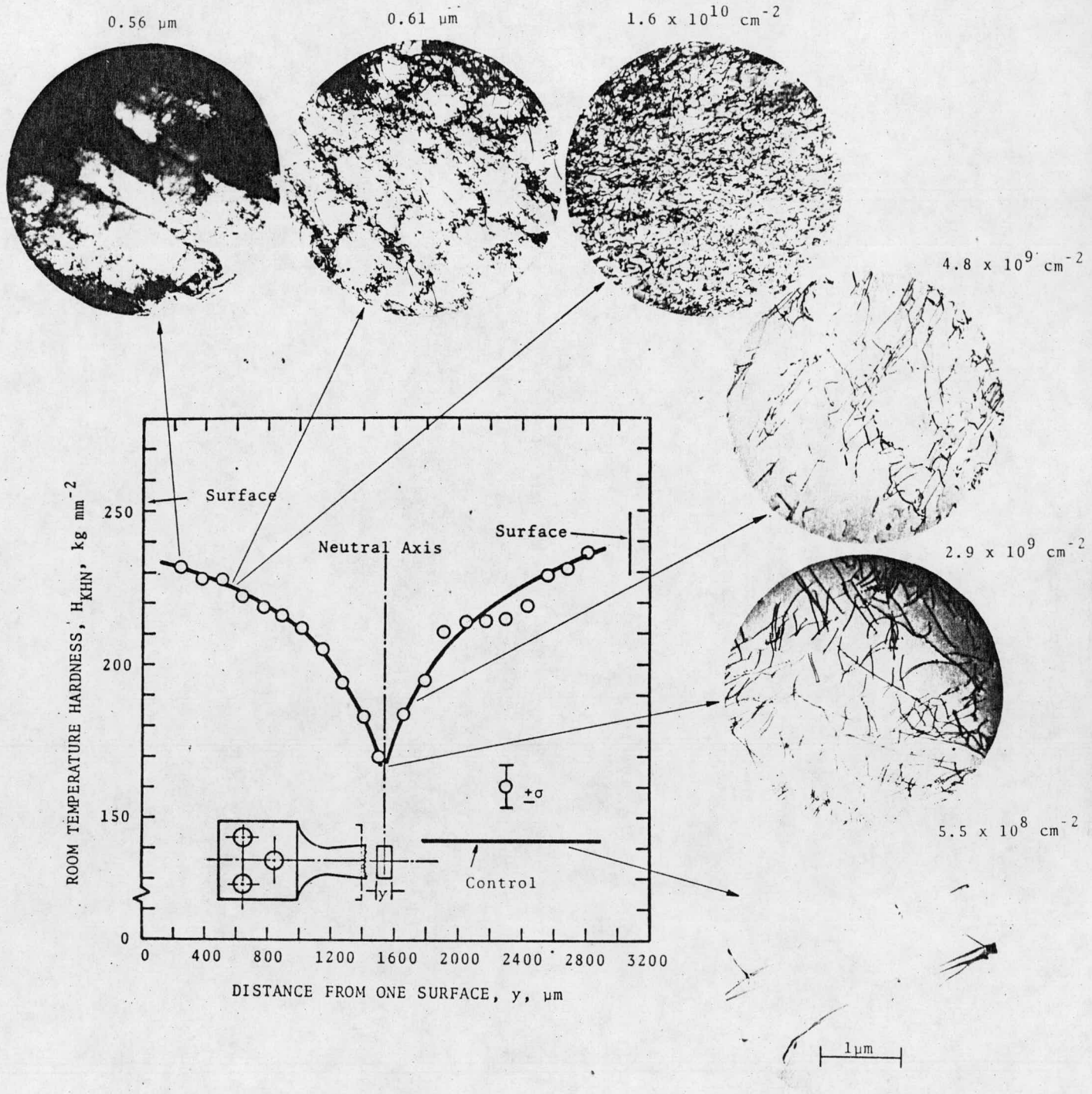

Fig. 27. Transverse Hardness Distribution in Incoloy 800 of Bend Fatigue Specimen on Plane Parallel to Fracture Surface with Corresponding Substructure.

Strain Rate: 4×10^{-3} sec^{-1}

Total Strain Range: 2 Percent

Fatigue Life: 260 Cycles, at 704°C

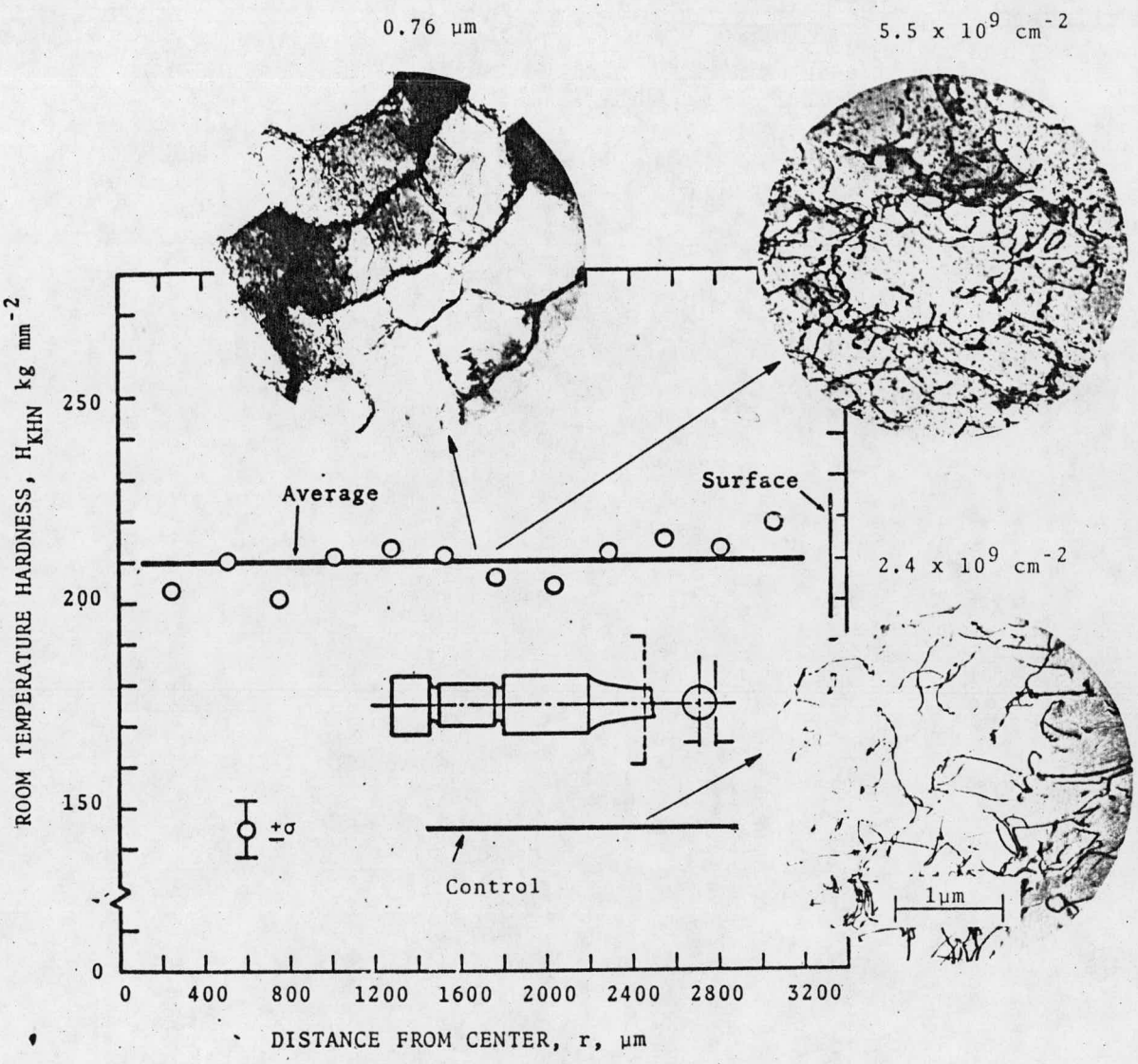

Fig. 28. Diametrical Hardness Distribution in Incoloy 800 of Push-Pull Fatigue Specimen on Plane Parallel to Fracture Surface with Corresponding Substructure.
Strain Rate: 4×10^{-3} sec^{-1}
Total Strain Range: 2 Percent
Fatigue Life: 407 Cycles, at 704°C

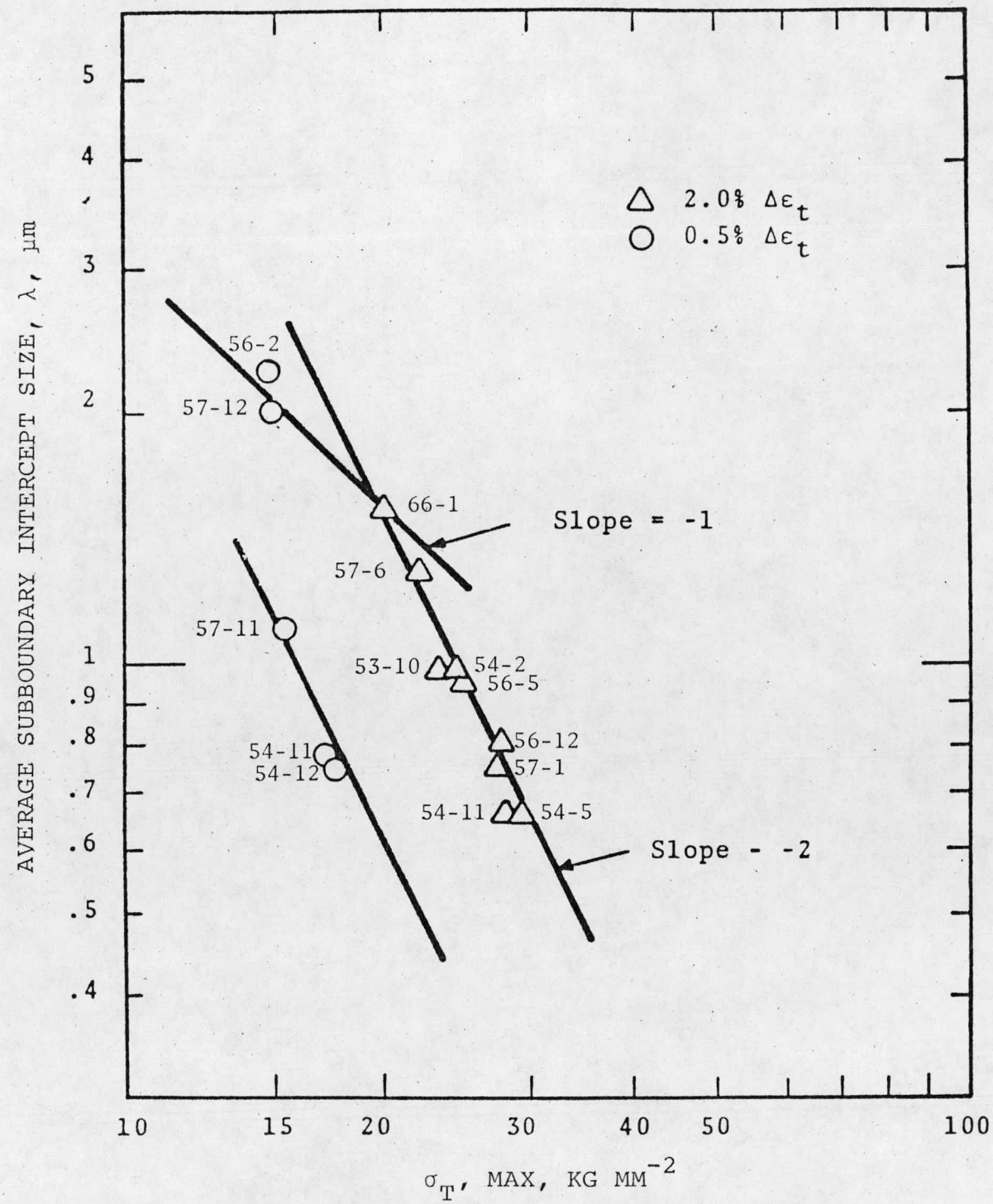

Fig. 29. Influence of Maximum Cyclic Tensile Stress on the Subboundary Intercept Size for 304 Stainless Steel Tested at 650°C in the Fatigue Mode with Various Tensile Hold Times.

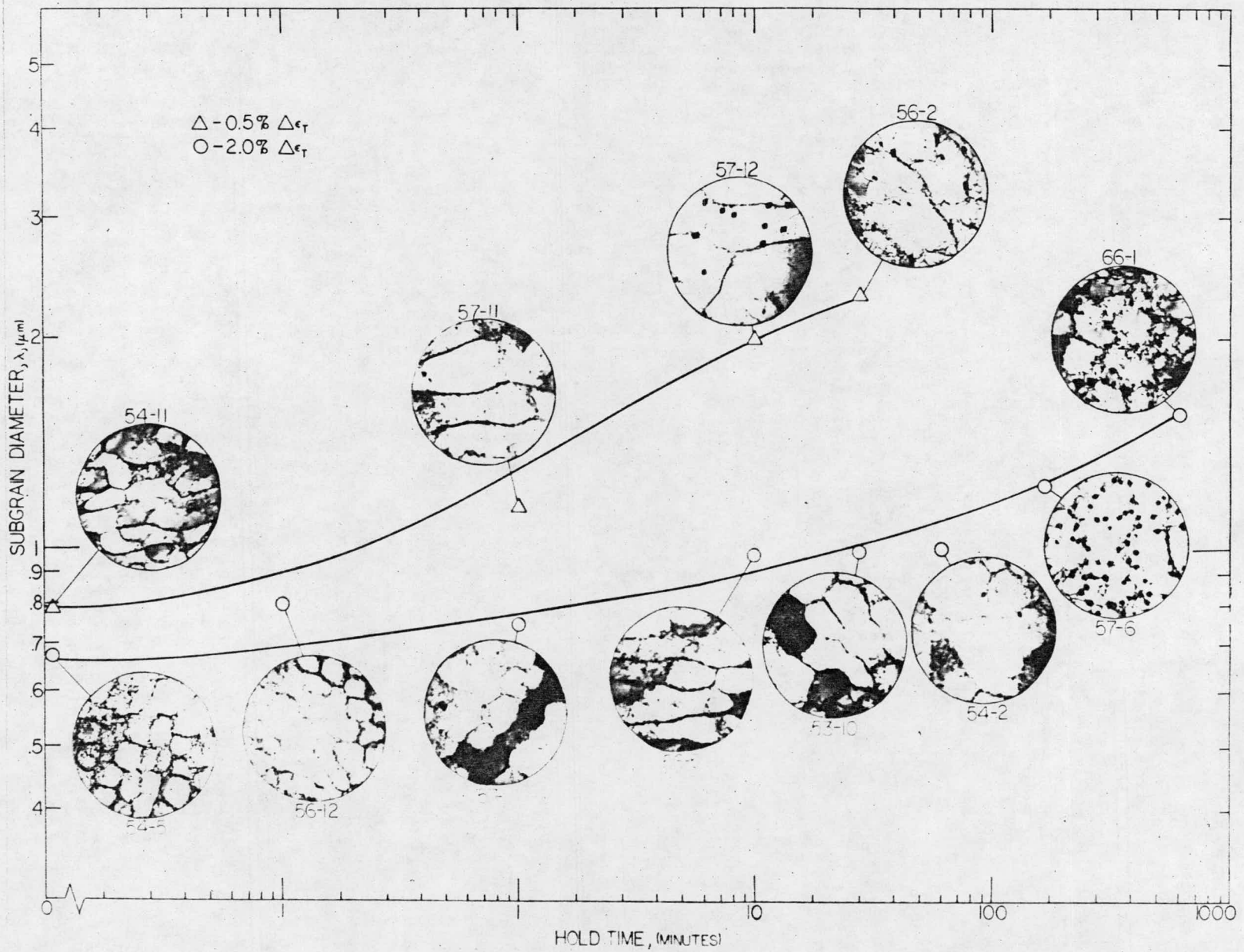

Fig. 30. Diagram-Plot of Characteristic Subgrain Diameters Associated With Various Tensile Hold Periods for 0.5% and 2.0% Total Strain Ranges

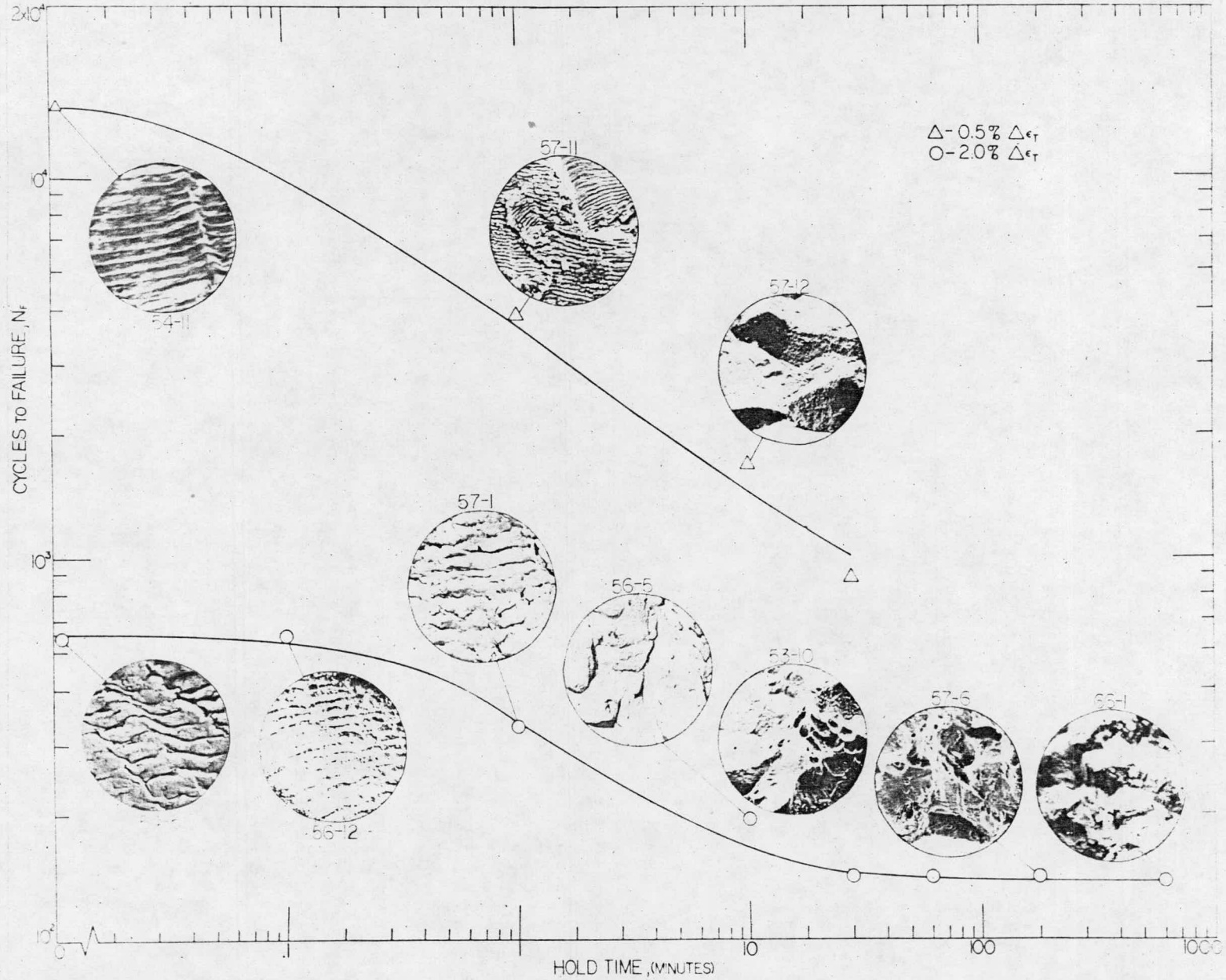

Fig. 31. Diagram-Plot of Cycles to Failure Versus Various Tensile Hold Periods for 0.5% and 2.0% Total Strain Ranges, Showing the Saturation in Cycles to Failure and the Transition from Transgranular to Intergranular Propagation With Increasing Tensile Hold Period.

APPENDIX I

LISTING OF PROGRESS REPORTS AND PAPERS PUBLISHED

Past Progress Reports

1. Progress Report, July 1, 1970 to December 31, 1970, COO-2107-1, February 16, 1971, University of Cincinnati, Cincinnati, OH.

2. Progress Report, January, February, March, 1971, COO-2107-2, May 12, 1971, University of Cincinnati, Cincinnati, OH.

3. Progress Report, April, May, June, 1971, COO-2107-3, August 31, 1971, University of Cincinnati, Cincinnati, OH.

4. Progress Report, July, August, September, 1971, COO-2107-4, October 25, 1971, University of Cincinnati, Cincinnati, OH.

5. Progress Report, October, November, December, 1971, COO-2107-5, February 15, 1972, University of Cincinnati, Cincinnati, OH.

6. Progress Report, January, February, March, 1972, COO-2107-6, May 15, 1972, University of Cincinnati, Cincinnati, OH.

7. Progress Report, April thru August, 1972, COO-2107-7, November 15, 1972, University of Cincinnati, Cincinnati, OH.

8. Progress Report, September thru December, 1972, COO-2107-8, March 15, 1973, University of Cincinnati, Cincinnati, OH.

9. Progress Report, January thru March, 1973, COO-2107-9, June 15, 1973, University of Cincinnati, Cincinnati, OH.

10. Progress Report, April thru December, 1973, COO-2107-10, March 15, 1974, University of Cincinnati, Cincinnati, OH.

Publications

1. Correlation Between Strain Hardening Parameters and Dislocation Substructure in Austenitic Stainless Steels, K. D. Challenger and J. Moteff, Scripta METALLURGICA 6, 155 (1972).

2. Characterization of the Deformation Substructure of AISI 316 Stainless Steel after High Strain Fatigue at Elevated Temperatures, K. D. Challenger and J. Moteff, Met. Trans. 3, 1677 (1972).

3. Quantitative Characterization of the Substructute of AISI 316 Stainless Steel Resulting From Creep, K. D. Challenger and J. Moteff, Met. Trans. 4, 749 (1973).

4. Correlation of Substructure with the Elevated Temperature Low Cycle Fatigue Properties of AISI 304 and 316 Stainless Steel, K. D. Challenger and J. Moteff, Published in the Proceedings of the Symposium on Fatigue at Elevated Temperatures - ASTM STP-520 (1973).

5. On the Influence of Deformation Rate on Intragranular Crack Propagation in Type 304 Stainless Steel, H. Nahm, D. J. Michel and J. Moteff, J. Mat. Sci. 8, 104 (1973).

6. Deformation Induced Twin-Boundary Crack Formation in Type 304 Stainless Steel, D. J. Michel, H. Nahm and J. Moteff, Mat. Sci. and Engrg. 11, 97 (1973).

7. Substructure of Type 316 Stainless Steel Deformed in Slow Tension at Temperatures Between 21° and 816°C, D. J. Michel, J. Moteff and A. J. Lovell, Acta Met. 21, 1269 (1973).

8. Reply to "Comments on 'On the Influence of Deformation Rate on Intragranular Crack Propagation in Type 304 Stainless Steel'", H. Nahm, D. J. Michel, and J. Moteff, J. Mat. Sci. 8, 1828 (1973).

9. A Correlation Between the Hot-Hardness and the Hot-Tensile Properties of AISI 304 Stainless Steel, J. Moteff and P. R. Sieber, Met. Trans. 5, 315 (1974).

10. Correlation of the Hot-Hardness with the Tensile Strength of 304 Stainless Steel to Temperatures of 1250°C, J. Moteff, R. K. Bhargava and W. L. McCullough, Met. Trans. 6A, 1101 (1975).

11. Some Aspects of Sub-Boundary and Mobile Dislocations During High Temperature Creep of AISI 316 and 304 Stainless Steel, V. K. Sikka, H. Nahm and J. Moteff, Mat. Sci. Eng. 20, 55 (1975).

12. The Role of Twin Boundary/Grain Boundary Intersections on Microcracking Behavior of AISI 304 Stainless Steel Deformed in Slow Tension and Creep at 650°C, H. Nahm and J. Moteff, J. Mat. Sci. 10, 1084 (1975).

13. Correlation of the Microstructure with the Creep and Tensile Properties of AISI 304 Stainless Steel, R. K. Bhargava, J. Moteff and R. W. Swindeman, in "Symposium on Structural Materials for Service at Elevated Temperatures in Nuclear Power Generation", ASME Winter Annual Meeting, Nov. 30 - Dec. 3, 1975, p. 31, Edited by A. O. Schaefer.

14. Second Phase Formation and Its Influence on the Fatigue Properties of Incoloy 800 at Elevated Temperature, H. Nahm and J. Moteff. Accepted for publication in Met. Trans.

15. Substructural Development During Low Cycle Fatigue of AISI 304 Stainless Steel at 649°C, H. Nahm, J. Moteff and D. R. Diercks, Submitted for Publication.

16. The Dislocation Substructure, Carbides and the Deformation Mechanism Map for AISI 304 Stainless Steel, R. K. Bhargava, J. Moteff and R. W. Swindeman, Accepted for Publication in Met. Trans.

Papers in Preparation

1. Quantitative Characterization of Substructure of Incoloy 800 Resulting from Low Cycle Fatigue at Elevated Temperatures, H. Nahm and J. Moteff.

2. Microcracking Behavior and Fracture of AISI 304 Stainless Steel at 650°C, H. Nahm and J. Moteff.

3. Fatigue Cracking and Striation Spacing in Incoloy 800 when Tested in the Bend and Push-Pull Modes, A. M. Ermi, H. Nahm and J. Moteff.

4. The Importance in the Substructure of Incoloy 800 in the Comparison of the Fatigue Properties When Tested in the Bend and Push-Pull Modes, H. Nahm, V. K. Sikka and J. Moteff.

5. Development of the Substructure of AISI 304 Stainless Steel as a Function of Creep Strain, R. K. Bhargava and J. Moteff.

6. Development of the Substructure of AISI 304 Stainless Steel Tested in Fatigue at 650°C with Hold Times, T. A. Kenfield and J. Moteff.

7. Substructure Development During Creep on Two Fe-Ni-Cr Alloys and a Ni-15Cr Alloy, C. G. Schmidt and J. Moteff.

8. Estimate of the Tensile Strength and the Activation Energy for Creep for Three Experimental Fe-Cr-Ni Alloys, C. G. Schmidt and J. Moteff.

9. Observation on Microcracking During Low Cycle Fatigue of AISI 304 Stainless Steel at 649°C, J. G. Costa, H. Nahm and J. Moteff.

10. Correlation of the Hot-Hardness with the Tensile Strength of the EBR-II XG05 Shrould Irradiated to 3.5×10^{22} n cm^{-2}, E > 0.1 MeV, J. Moteff.

11. Intragranular Deformation Behavior of AISI 304 Stainless Steel at Elevated Temperature, H. Nahm and J. Moteff.

12. On the Activation Energy for Creep of AISI 304 Stainless Steel, R. K. Bhargava and J. Moteff.

13. The Influence of Dislocation Cells on the Creep of AISI 304 Stainless Steel, R. K. Bhargava and J. Moteff.

14. Substructure Strengthening in Some Austenitic Stainless Steels, R. K. Bhargava, H. Nahm and J. Moteff.

15. The Effect of Temperature on the Fatigue Crack Initiation and Propagation in LCF of AISI 304 Stainless Steel, J. D. Moteff and J. Moteff.

DISTRIBUTION LIST

U. S. ENERGY RESEARCH & DEVELOPMENT ADMINISTRATION

Division of Reactor Development and Demonstration

1 - Deputy Director for Development and Technology

1 - Assistant Director for Technology

2 - Chief, Fuel Systems Branch

1 - Chief, Materials Development Branch

1 - Assistant Director for Engineering

1 - Chief, Materials & Structures Branch

Division of Controlled Thermonuclear Research

1 - Director, Division of Controlled Thermonuclear Research

1 - Assistant Director for Development and Technology

Division of Physical Research

1 - Director, Division of Physical Research

1 - Assistant Director for Material Sciences

Chicago Operations Office

1 - Director, Chicago Operations Office

ARGONNE NATIONAL LABORATORY

1 - Manager, Advanced Fuel Systems

GENERAL ELECTRIC - FBRD

1 - Manager, Program Management

NAVAL RESEARCH LABORATORY

1 - Head, Thermostructural Materials Branch, Code 6390

OAK RIDGE NATIONAL LABORATORY

1 - Manager, LMFBR Fuels and Materials Program

WESTINGHOUSE - ADVANCED REACTORS DIVISION

1 - Manager, Technology

HANFORD ENGINEERING DEVELOPMENT LABORATORY

2 - Manager, Materials Engineering

STANFORD UNIVERSITY

1 - Oleg Sherby

DISTRIBUTION LIST

U. S. ENERGY RESEARCH & DEVELOPMENT ADMINISTRATION

Division of Reactor Development and Demonstration

1 - Deputy Director for Development and Technology

1 - Assistant Director for Technology

2 - Chief, Fuel Systems Branch

1 - Chief, Materials Development Branch

1 - Assistant Director for Engineering

1 - Chief, Materials & Structures Branch

Division of Controlled Thermonuclear Research

1 - Director, Division of Controlled Thermonuclear Research

1 - Assistant Director for Development and Technology

Division of Physical Research

1 - Director, Division of Physical Research

1 - Assistant Director for Material Sciences

Chicago Operations Office

1 - Director, Chicago Operations Office

ARGONNE NATIONAL LABORATORY

1 - Manager, Advanced Fuel Systems

GENERAL ELECTRIC - FBRD

1 - Manager, Program Management

NAVAL RESEARCH LABORATORY

1 - Head, Thermostructural Materials Branch, Code 6390

OAK RIDGE NATIONAL LABORATORY

1 - Manager, LMFBR Fuels and Materials Program

WESTINGHOUSE - ADVANCED REACTORS DIVISION

1 - Manager, Technology

HANFORD ENGINEERING DEVELOPMENT LABORATORY

2 - Manager, Materials Engineering

STANFORD UNIVERSITY

1 - Oleg Sherby